

Electronic Theses and Dissertations, 2004-2019

2013

Interdiffusion Reaction Between Uranium-zirconium And Iron

Young Joo Park
University of Central Florida

 Part of the [Materials Science and Engineering Commons](#)
Find similar works at: <https://stars.library.ucf.edu/etd>
University of Central Florida Libraries <http://library.ucf.edu>

This Masters Thesis (Open Access) is brought to you for free and open access by STARS. It has been accepted for inclusion in Electronic Theses and Dissertations, 2004-2019 by an authorized administrator of STARS. For more information, please contact STARS@ucf.edu.

STARS Citation

Park, Young Joo, "Interdiffusion Reaction Between Uranium-zirconium And Iron" (2013). *Electronic Theses and Dissertations, 2004-2019*. 2675.
<https://stars.library.ucf.edu/etd/2675>

**INTERDIFFUSION REACTION BETWEEN URANIUM-ZIRCONIUM
ALLOY AND IRON**

by

YOUNG JOO PARK
B.S. Hanyang University, 2003
M.S. Hanyang University, 2005

A thesis submitted in partial fulfillment of the requirements
for the degree of Master of Science
in the Department of Materials Science and Engineering
in the College of Engineering and Computer Science
at the University of Central Florida
Orlando, Florida

Summer Term
2013

Major Professor: Yongho Sohn

© 2013 Young Joo Park

ABSTRACT

U-Zr metallic fuels clad in Fe-alloys are being considered for application in an advanced Sodium-Cooled Fast Reactor (SFR) that can recycle the U-Zr fuels and minimize the long-lived actinide waste. To understand the complex fuel-cladding chemical interaction of the U-Zr metallic fuel with Fe-alloys, a systematic multicomponent diffusion study was carried out using solid-to-solid diffusion couples. The U-10 wt.% Zr vs. pure Fe diffusion couples were assembled and annealed at temperatures, 630, 650 and 680°C for 96 hours. Development of microstructure, phase constituents, and compositions developed during the thermal anneals were examined by scanning electron microscopy, transmission electron microscopy and X-ray energy dispersive spectroscopy. A complex microstructure consisting of several layers that include phases such as U_6Fe , UFe_2 , $ZrFe_2$, α -U, β -U, Zr-precipitates, χ , ϵ , and λ was observed. Multi-phase layers were grouped based on phase constituents and microstructure, and the layer thicknesses were measured to calculate the growth constant and activation energy. The local average compositions through the interaction layer were systematically determined, and employed to construct semi-quantitative diffusion paths on isothermal U-Zr-Fe ternary phase diagrams at respective temperatures. The diffusion paths were examined to qualitatively estimate the diffusional behavior of individual components and their interactions. Furthermore, selected area diffraction analyses were carried out to determine, for the first time, the exact crystal structure and composition of the χ , ϵ and λ -phases. The χ , ϵ and λ -phases were identified as $Pnma(62) Fe(Zr,U)$, $I4/mcm(140) Fe(Zr,U)_2$, and $I4/mcm(140) U_3(Zr,Fe)$, respectively.

I dedicate this work to my family, and especially my advisor, Dr. Yongho Sohn. Thank you for your never-ending support, love and guidance.

ACKNOWLEDGMENTS

This work was financially supported by Idaho National Laboratory (Contract No. 00095398) under the operation of U.S. Department of Energy – Battelle Energy Alliance, LLC (DE-AC07-051D14517). I would like to thank Dr. Yong-ho Sohn, the chair of the thesis committee for his support, encouragement and advice throughout my career at the University of Central Florida (UCF). Financial support and technical collaboration with Dr. Bulent H. Sencer and Dr. John Rory Kennedy at Idaho National Laboratory are sincerely appreciated. I would like to express my gratitude to the committee members, Dr. Kevin Coffey and Dr. Jiyu Fang for the education and training they provided me and for taking the time to examine and critique this document. I would also like to thank all faculty and staff of the Advanced Materials Processing and Analysis Center (AMPAC) for their teachings and support throughout my years of study.

TABLE OF CONTENTS

LIST OF FIGURES	viii
LIST OF TABLES	xi
CHAPTER 1: INTRODUCTION	1
CHAPTER 2: LITERATURE REVIEW	3
2.1. Sodium-Cooled Fast Reactor	3
2.2. Fuel Cladding Chemical Interaction	6
2.2.1. Interdiffusion and Reaction in Binary U vs. Fe	7
2.2.2. Interdiffusion and Reaction in U-Zr-Fe Ternary System	7
CHAPTER 3: EXPERIMENTAL PROCEDURE	10
3.1. Laboratory Facility	10
3.2. Alloy Preparation and Diffusion Experiment	13
3.3 Characterization	15
CHAPTER 4: RESULTS AND DISCUSSION	18
4.1. Microstructural and Compositional Development.....	18
4.2. Diffusion Path of U-Zr vs. Fe System	25
4.3. Growth of Interdiffusion Microstructure in U-10 wt.% Zr vs. Fe Diffusion Couples.....	31
4.4. Crystallographic Analysis of Ternary Intermetallic Phases	35
CHAPTER 5: SUMMARY.....	43

APPENDIX: MATHEMATICAL THEOREM FOR RECIPROCAL LATTICE	45
REFERENCE.....	50

LIST OF FIGURES

Figure 1. The sequence of breeding reaction that converts ^{238}U to fissionable ^{239}Pu	5
Figure 2. A schematic diagram of a SFR system [3].....	5
Figure 3. Glove box under a controlled Ar atmosphere.....	11
Figure 4. A schematic diagram of gas flow for alloy handling.	11
Figure 5. High vacuum system for evacuating quartz capsules.....	12
Figure 6. Lindberg/Blue TM three-zone tube furnace	12
Figure 7. The compositional evaluation of U-10 wt.% Zr alloy before and after diffusion experiments.....	13
Figure 8. Quartz capsules for heat treatment of diffusion couples.	15
Figure 9. (a) Zeiss ULTRA-55 FEG SEM (b) FEI TEM200 FIB (c) FEI TECNAI F30 TEM. ...	16
Figure 10. FIB sample preparation: (a) initial milling completion (b) in-situ lift-out (c) insertion of sample onto the pre-slotted Cu-grid (d) welding the sample on Cu-grid.	17
Figure 11. BSE micrographs of U-10 wt.% Zr vs. Fe diffusion couple annealed at 630°C for 96 hours.	19
Figure 12. BSE micrographs of U-10 wt.% Zr vs. Fe diffusion couple annealed at 650°C for 96 hours.	20
Figure 13. BSE micrographs of U-10 wt.% Zr vs. Fe diffusion couple annealed at 680°C for 96 hours.	21
Figure 14. The isothermal ternary phase diagram of U-Zr-Fe system at 700°C [14].....	24
Figure 15. XEDS mapping for U, Zr and Fe in the U-10 wt.% Zr vs. Fe diffusion couple	

annealed at 680°C for 96 hours.	25
Figure 16. Estimated diffusion path of U-Zr vs. Fe diffusion couple annealed at 630°C for 96 hours plotted on the isothermal ternary phase diagram of the U-Zr-Fe system.	27
Figure 17. Estimated diffusion path of U-Zr vs. Fe diffusion couple annealed at 650°C for 96 hours plotted on the isothermal ternary phase diagram of the U-Zr-Fe system.	28
Figure 18. Estimated diffusion path of U-Zr vs. Fe diffusion couple annealed at 680°C for 96 hours plotted on the isothermal ternary phase diagram of the U-Zr-Fe system.	29
Figure 19. Thicknesses of each distinguished layer developed in diffusion couples, U-10 wt.% Zr vs. Fe diffusion couples annealed at 630, 650 and 680°C for 96 hours.	32
Figure 20. Arrhenius plot of parabolic growth constant for each interdiffusion layer from diffusion couples, U-10 wt.% Zr vs. Fe diffusion couples annealed at 630, 650 and 680°C for 96 hours.	34
Figure 21. U-Zr vs. Fe diffusion couples annealed at 680°C for 96 hours: (a) typical BSE micrograph and FIB preparations for TEM studies (b) for χ phase and several layers near Fe side, (c) for χ and ϵ phase, and (d) ϵ and λ phase.....	36
Figure 22. The χ phase developed in the U-Zr vs. Fe diffusion couple annealed at 680°C: (a) HAADF STEM micrograph, (b) DF micrograph, and (c) SAED along the 1 1 1, and (d) 5 1 3 beam directions.	38
Figure 23. The ϵ phase developed in the U-Zr vs. Fe diffusion couple annealed at 680°C: (a) HAADF STEM micrograph, (b) DF micrograph, and (c) SAED along the 1 1 1 and (d) 0 1 2 beam directions.	39

Figure 24. The λ phase developed in the U-Zr vs. Fe diffusion couple annealed at 680°C: (a) HAADF STEM micrograph, (b) DF micrograph, and (c) SAED along the 2 1 2 and (d) 1 1 0 beam directions. 40

Figure 25. The procedure C++ coding for the identification of crystal structure and indexing ... 49

LIST OF TABLES

Table 1. Thermal neutron capture cross sections for potential coolants of fast reactors. [7].....	4
Table 2. Average composition of each phase observed in diffusion couple annealed at 680°C in this study (Unit: at.%).....	22
Table 3. Phases and phase number for each section of the diffusion path corresponding to the microstructure annealed at 630°C for 96 hours.....	30
Table 4. Phases and phase number for each section of the diffusion path corresponding to the microstructure annealed at 650°C for 96 hours.....	30
Table 5. Phases and phase number for each section of the diffusion path corresponding to the microstructure annealed at 680°C for 96 hours.....	31
Table 6. Phases in reaction layers distinguished for determination of growth constants.	32
Table 7. Thicknesses of each interdiffusion layer measured from diffusion couples, U-10 wt.% Zr vs. Fe diffusion couples annealed at 630, 650 and 680°C for 96 hours.	34
Table 8. The growth constants and activation energies of each interdiffusion layer from diffusion couples, U-10 wt.% Zr vs. Fe diffusion couples annealed at 630, 650 and 680°C for 96 hours.	35
Table 9. Crystallographic information of the χ , ε and λ phases.	41
Table 10. Chemical composition measured by SEM-XEDS and TEM-XEDS for the χ , ε and λ phases (unit: at.%).	42

LIST OF ABBREVIATIONS

BSC	Backscattered Electron Micrograph
DF	Dark Field imaging
DU	Depleted Uranium
EDS/XEDS	Energy Dispersive X-Ray Spectroscopy
FCCI	Fuel-Cladding Chemical Interaction
FIB	Focused Ion Beam
Gen-IV	Generation IV
HAADF	High-Angle Annular Dark-Field
SAED	Selected Area Electron Diffraction
SE	Secondary Electron imaging
SEM	Scanning Electron Microscope
SFR	Sodium-Cooled Fast Reactor
STEM	Scanning Transmission Electron Microscopy
TEM	Transmission Electron Microscopy
XEDS	X-ray Energy Dispersive Spectroscopy
XRD	X-ray Diffraction
ZAF	Atomic number, Absorption and Fluorescence correction

CHAPTER 1: INTRODUCTION

Uranium (U) – Zirconium (Zr) metallic fuel with Plutonium (Pu) and minor actinides has been considered as the main fuel alloy for the Generation IV (Gen-IV) Nuclear Energy systems [1]. The goals of the Gen-IV system include reducing radiotoxicity in the repositories and the amount of radioactive waste. Another goal is to utilize the energy content of the spent nuclear fuel. To meet these goals, the Sodium-Cooled Fast Reactor (SFR) is utilized. The SFR is one of several models for the Gen-IV systems [2] [3]. The SFR, which is normally operated at the high temperature of approximately 550°C, employs liquid sodium (Na) as the main coolant. The SFR minimizes long-lived actinide waste through treatment, and re-uses the spent uranium resources. U-Zr alloys have been considered for SFR fuels. When Zr is alloyed in U for the metallic nuclear fuel, it mitigates the chemical interaction between the fuel and cladding materials (e.g., typically Fe-based alloys), and elevates the alloy solidus temperature [4]. However, during irradiation, the U-Zr alloy can swell and make contact with the cladding, causing metallurgical interactions to occur at the fuel-cladding interface, termed fuel-cladding chemical interaction (FCCI). The FCCI can change the microstructure, phase constituents and composition near the vicinity of the fuel-cladding interface, and can adversely affect the fuel performance and structural integrity of the cladding alloy. Additional consideration must be given to the constituent redistribution within the fuel alloy due to temperature gradient that leads to the reduction of Zr content towards the center of the fuel [5].

A thorough understanding of the interdiffusion and reaction between the fuel alloy and

the cladding materials is necessary to optimize and predict the reactor performance. This thesis therefore examines the interdiffusion behavior between the U-10 wt.% Zr fuel and pure Fe cladding in terms of microstructure, diffusion paths, and phase constituents by using solid-to-solid diffusion couples. The U-10 wt.% Zr vs. pure Fe diffusion couples were assembled, annealed at temperatures, 630, 650 and 680°C for 96 hours and examined by scanning electron microscopy (SEM), transmission electron microscopy (TEM) and X-ray energy dispersive spectroscopy (XEDS). Analyses were carried out to determine the growth rate of interdiffusion microstructure and diffusion paths on isothermal U-Zr-Fe ternary phase diagrams at respective temperatures. Furthermore, for the first time, the exact crystal structure and composition of χ , ε and λ -phases were identified as Pnma(62) Fe(Zr,U), I4/mcm(140) Fe(Zr,U)₂, and I4/mcm(140) U₃(Zr,Fe), respectively.

CHAPTER 2: LITERATURE REVIEW

2.1. Sodium-Cooled Fast Reactor

The SFR system is one of Gen-IV reactors to be designed as an advanced fast neutron reactor, and has the fuel breeding capability [6]. Liquid Na contained in the SFR reactor vessel is used to cool the reactor and to exchange the thermal energy to generate the electricity. Na has appropriate properties [6] to be the coolant for fast reactors as listed below:

- Thermal conductivity (142 W/m/K)
- Relatively low density (0.927 g/cm³ at 1atm)
- Relatively large liquid range (97.72 ~ 883°C)
- Relatively low thermal neutron capture cross section (0.53 barns)

In order to cool the core of a fast reactor, coolant with higher thermal conductivity than water is required, because the fast reactor's power density of ~250 kW/l is much larger than the widely-accepted light water reactor with power density of 50 ~ 100 kW/l. The fact that liquid Na has lower density than water makes it easy to circulate and exchange the heat generated by fission. The general operating temperature of 550°C for SFR is between the melting point $T_m=97.72^\circ\text{C}$ and boiling point $T_b=883^\circ\text{C}$ of Na. Also, the thermal neutron capture cross section of Na is relatively low among the potential liquid coolant for fast reactor as listed in Table 1. A small module SFR produces 50 MWe, and large size SFR can generate up to 1,500 MWe. Metallic fuel or oxide fuels have been considered as the main fuel.

Table 1. Thermal neutron capture cross sections for potential coolants of fast reactors. [7]

Element	Thermal neutron capture cross section (barns)
Hg	372.3±4.0
K	2.1 ± 0.1
Rb	0.38 ± 0.04
Na	0.53 ± 0.005
Pb	0.138 ± 0.004
Li	0.0449 ± 0.003
Bi	0.0338 ± 0.0007

The reactor vessel utilizes almost all energy in the natural U. U, as found in nature, is a mixture of three types of isotopes, 99.284% ^{238}U , 0.711% ^{235}U and 0.0055% ^{234}U . Generally, fissionable reactor fuel consists of ^{235}U , but unfortunately, non-fissionable ^{238}U is the most common naturally occurring isotope. The ^{238}U cannot sustain the chain reaction needed for nuclear energy generation using commercial reactors. Figure 1 shows the main sequence of breeding reaction for sustaining fission within the SFR. The neutrons caused by fission reactions breed more fuel from non-fissionable isotopes. The ^{238}U , which absorbs the neutron, is converted to ^{239}U , and then the two β -decay eventually converts the non-fissionable ^{238}U to fissionable ^{239}Pu . Figure 2 shows a schematic diagram of a SFR nuclear system.

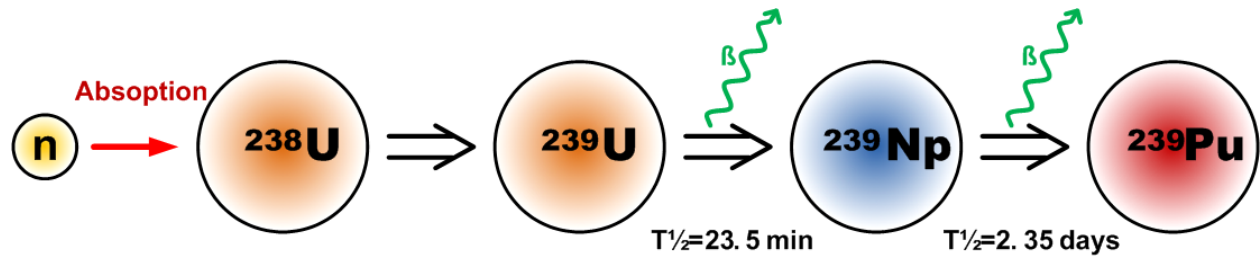


Figure 1. The sequence of breeding reaction that converts ${}^{238}\text{U}$ to fissionable ${}^{239}\text{Pu}$.

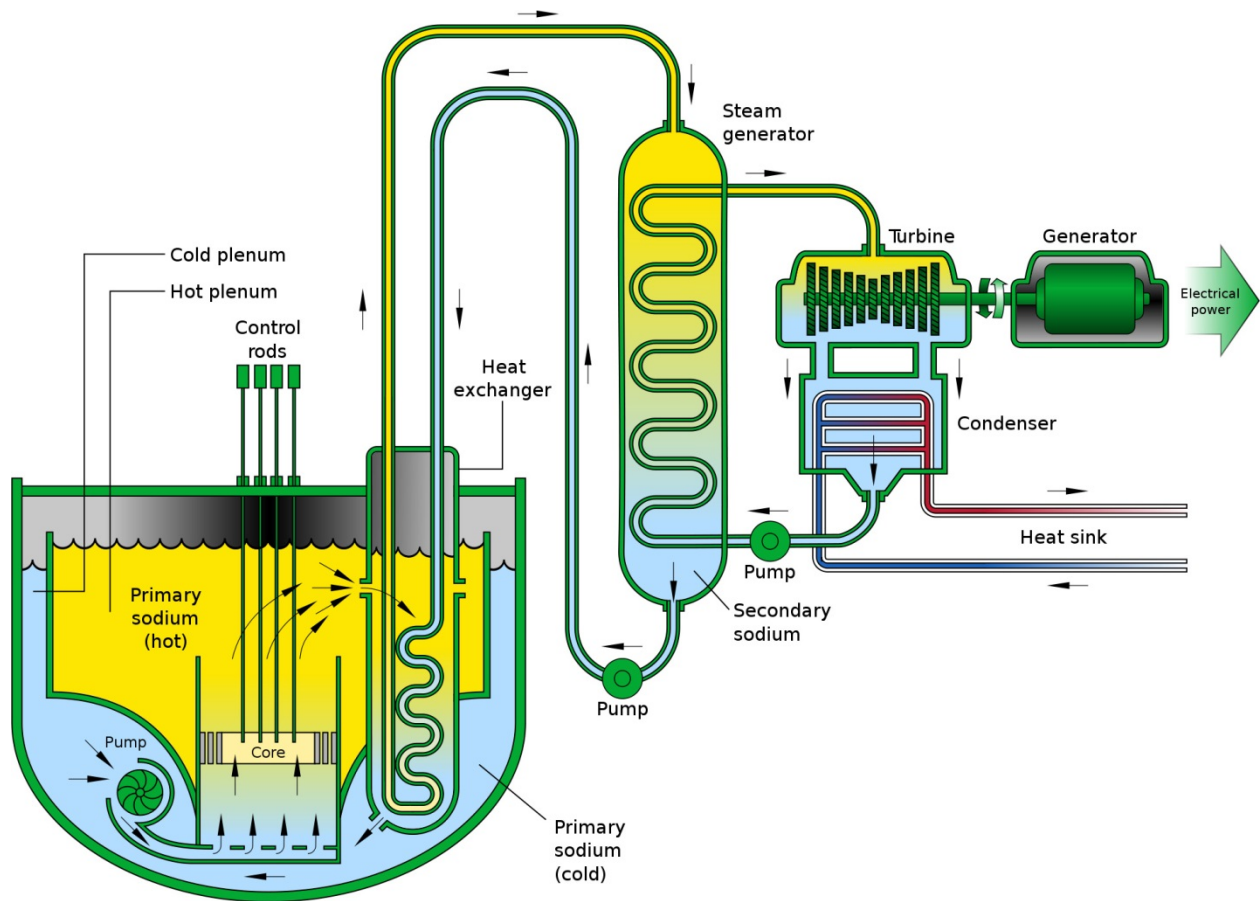


Figure 2. A schematic diagram of a SFR system [3].

2.2. Fuel Cladding Chemical Interaction

Although metallic fuels have been considered as an ideal fuel for fast reactors, few potential disadvantages have been reported for application in fast reactors. Among them, the fuel cladding chemical interaction (FCCI) has been identified as a critical factor that can adversely affect the performance and reliability of the fuels. During the operation, metallic fuels can swell (i.e., volumetric expansion) due to neutron irradiation, and contact the cladding alloys, typically Fe-base alloys. This contact between the fuel and cladding can then induce the interdiffusion [8-13], alter the composition, microstructure and properties of both the fuel and cladding, and can cause a premature breach of a fuel element including formation of low-melting phases. Therefore, in order to design and implement fast reactors with metallic fuels, it is important to understand the diffusion behavior between the metallic fuels and various cladding alloys based on Fe. An ideal cladding material for metallic fuel system requires:

- Good thermal conductivity
- Low neutron absorption cross section
- Good chemical resistant
- High melting point
- Low thermal expansion coefficient
- Low diffusivity between fuel and cladding

2.2.1. Interdiffusion and Reaction in Binary U vs. Fe

Previous investigation by Huang *et al.* [8] on the U-Fe binary system serves as the basis for quantitative and qualitative effects of alloying additions, Zr in the U, and assist in understanding the FCCI process between the U-Zr metallic nuclear fuels and Fe-cladding alloy. There were four phases observed in the U vs. Fe diffusion couples annealed in the temperature range of 580°C to 700°C, which were U (<668°C, α -U; 668-776°C, β -U; >776°C, γ -U), U_6Fe (tI28), UFe_2 (cF24) and α -Fe (cI2) [14]. The interfaces between phases had uniform thicknesses and the solubility ranges of the two intermetallic phases, U_6Fe and UFe_2 , were negligible. The difference between the extrinsic and intrinsic growth constants of the UFe_2 phase indicated that the growth of UFe_2 was impeded by the faster growing U_6Fe phase, but U_6Fe was hardly affected by the growth of the UFe_2 phase. Also, in Huang's study [8] it is suggested that the allotropic transformation of U from α -U (orthorhombic) to β -U (tetragonal) slightly affected the growth of the U_6Fe phase.

2.2.2. Interdiffusion and Reaction in U-Zr-Fe Ternary System

Ogata [10] carried out interdiffusion experiments isothermally using diffusion couples of U-Zr vs. Fe annealed at 923 K as a function of time. The diffusion-controlled reaction zone between the U-Zr and Fe alloys were distinguished into several layers: layer A (UFe_2), layer B ($U_6Fe+UFe_2$), layer C ($ZrFe_2$), layer D ($U_6Fe+ZrFe_2$), layer E ($U_6Fe+\epsilon$) and layer F (α -U+ λ). Ogata [10] reported unknown ternary intermediate phases, named ϵ and λ , from the

microstructural analyses of the diffusion zone. Also, Ogata [10] explained that these layers are similar to Keiser's observations [11, 12] on interdiffusion layers between U-Pu-Zr and HT9: $(\text{U,Pu,Zr})(\text{Fe,Cr})_2$, $(\text{U,Pu,Zr})_6(\text{Fe,Cr}) + (\text{U,Pu,Zr})(\text{Fe,Cr})_2$, $(\text{Zr,U,Pu})(\text{Fe,Cr})_2$, $(\text{Zr,U,Pu})(\text{Fe,Cr})_2 + (\text{U,Pu,Zr})_6(\text{Fe,Cr})$. Keiser concluded that presence of Ni and Cr significantly influences the diffusional interaction between U-Zr alloy and HT9. In particular U was observed to diffuse much faster within the intermetallics containing Ni than those without Ni, and the Cr was associated with formation of Zr-rich precipitates.

Nakamura [13] investigated the isothermal solid-state reactions in the U-Zr-Fe system using solid-to-solid diffusion couples of U-Zr vs. Fe. The microstructure shows the multi-layer reaction zone. Each layer consisted of one or two phases: UFe_2 , $\text{U}_6\text{Fe}+\text{UFe}_2$, ZrFe_2 , $\text{U}_6\text{Fe}+\chi$, $\text{U}_6\text{Fe}+\varepsilon$, $\alpha\text{-U}+\varepsilon$ and $\alpha\text{-U}+\lambda$ at 908K and 923K; UFe_2 , $\text{U}_6\text{Fe}+\text{UFe}_2$, ZrFe_2 , $\text{U}_6\text{Fe}+\chi$, $\text{U}_6\text{Fe}+\varepsilon$, $\beta\text{-U}+\varepsilon$ and $\beta\text{-U}+\lambda$ at 973K. The χ (U-32Zr-50Fe), ε (U-(30~50)Zr-33Fe) and λ (U-(21~25)Zr-6Fe) phases reported by Nakamura [13] were ternary compounds. The thickness of the interdiffusion layers increased approximately in proportion to the parabolic time, as in the case of diffusion-controlled process. On the U-Zr side of the interdiffusion reaction zone, the estimated diffusion path remained the same regardless of annealing temperatures. It means the constitution, phases, and diffusional behavior of U, Zr and Fe did not change significantly from 908K to 988K. On the other hand, the estimated diffusion paths varied as a function of annealing temperature for the Fe side. The composition of diffusion paths at 908K and 923K went through the three-phase (U_6Fe , UFe_2 and ZrFe_2) region on the ternary isotherm, but the diffusion paths of above 973K were estimated to pass through the two-phase (UFe_2 and ZrFe_2) region. Nakamura explained the

potential variation in the formation energy of the U_6Fe , UFe_2 and $ZrFe_2$ phases to discuss this difference in diffusion paths.

CHAPTER 3: EXPERIMENTAL PROCEDURE

3.1. Laboratory Facility

All alloys were continuously handled under an Ar atmosphere in a glove box shown in Figure 3 to minimize oxidation of U-10 wt.% Zr alloys and to prevent contamination of the laboratory facility. Figure 4 shows a schematic diagram of the Ar-gas flow. The inert atmosphere is maintained by Ar-gas injected into the glove box through an outlet. The Ar-gas exited the glove box through oil in a flask and an air filter to trap potential airborne particles, and exhausted through a fume hood. The high vacuum system shown in Figure 5 was utilized for evacuating quartz capsules and flushing H₂-gas and Ar-gas to be presented in Section 3.2. The Lindberg/BlueTM three-zone tube furnace shown in Figure 6 was used to anneal at homogeneous temperatures for predetermined times to be presented in Section 3.2.

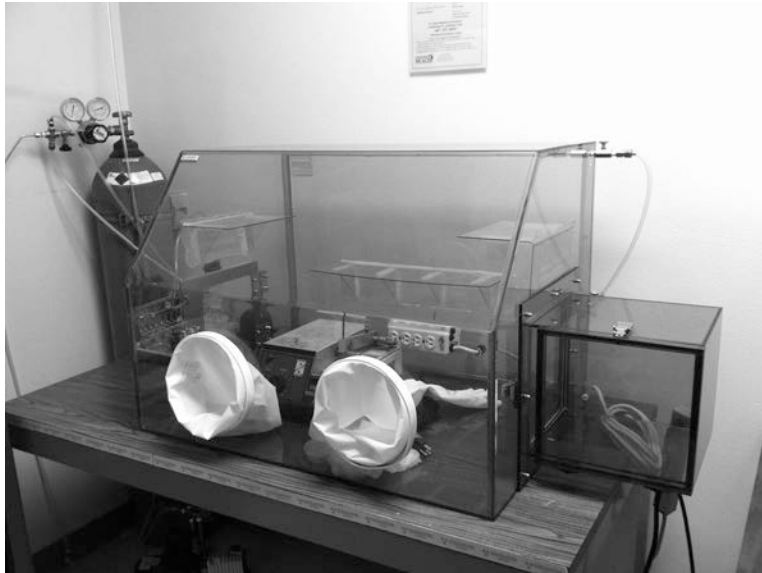


Figure 3. Glove box under a controlled Ar atmosphere.

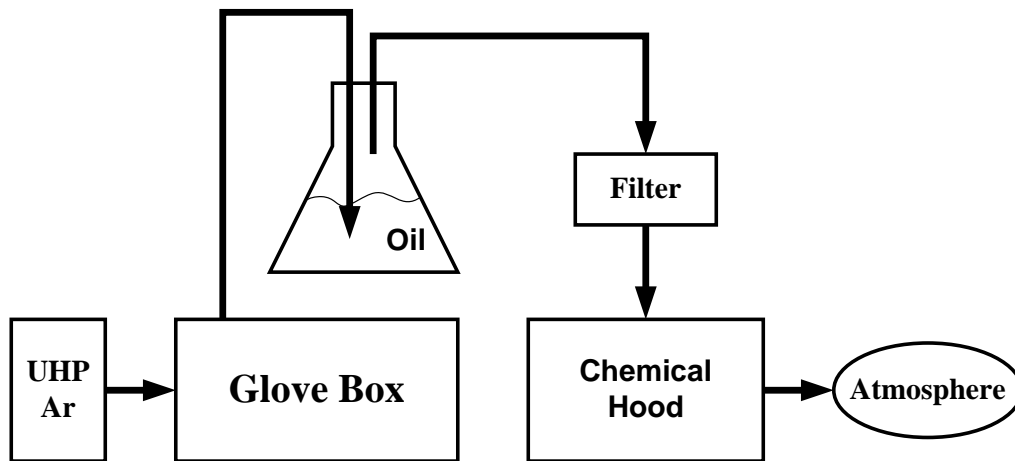


Figure 4. A schematic diagram of gas flow for alloy handling.



Figure 5. High vacuum system for evacuating quartz capsules.



Figure 6. Lindberg/Blue™ three-zone tube furnace

3.2. Alloy Preparation and Diffusion Experiment

The U-10 wt.% Zr alloys were cast via arc melting by Idaho National Laboratory. They were melted three times to ensure homogeneity and then drop-cast to form rods with 12.7 mm diameter. All U-Zr alloys were handled in the glove box as described before. Fe rods of 99.99% purity were obtained from a commercial source (Alpha-AesarTM). Figure 7 shows average composition of U-10 wt.% Zr alloys before and after diffusion anneal experiments at various temperatures. The composition remains uniform.

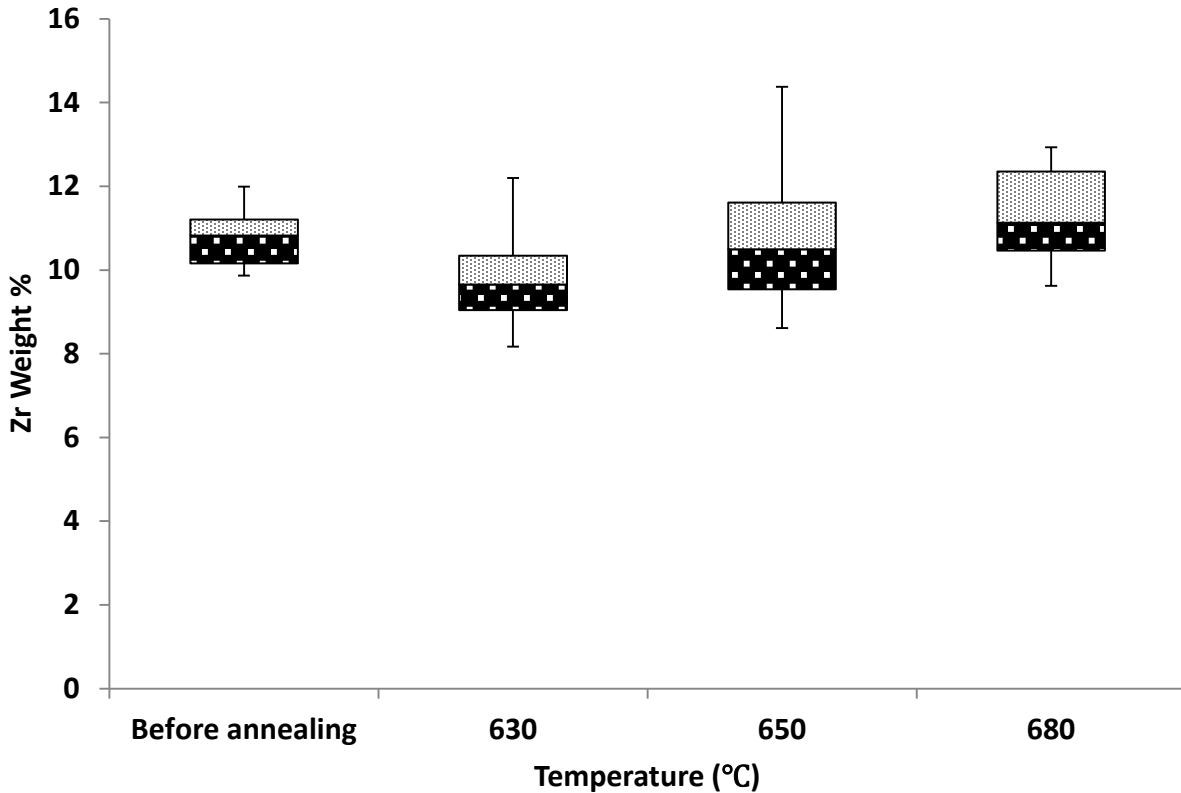


Figure 7. The compositional evaluation of U-10 wt.% Zr alloy before and after diffusion experiments.

U-Zr alloys and pure Fe were sectioned into disks of about 3mm in thickness, and the surface of disks designated to form diffusion interface were polished using silicon carbide papers (240, 600, 800 and 1200 grit) with ethanol as a lubricant for minimizing oxidation.

Figure 8 shows the U-Zr alloy vs. Fe alloy couples clamped by a steel jig with alumina disks to prevent interaction between the diffusion couple disks and the steel jig set. The assembled diffusion couples were encapsulated in quartz capsules with a piece of Ta foil, and then were repeatedly flushed with H₂-gas and Ar-gas. The tubes were then sealed under vacuum ($\sim 10^6$ torr) by using an oxygen-propane torch. Figure 8 shows diffusion couples before and after being sealed in quartz tubes. Each sealed couple was annealed in a Lindberg/BlueTM three-zone tube furnace at 630, 650 and 680°C for 96 hours. After heat treatment, each couple was pulled out of the furnace, and then immediately quenched by breaking the quartz capsule in cold water. Each couple was submerged for about 1 minute in water, and then the diffusion couples were extracted from the quartz capsule. The diffusion couples were mounted in epoxy and cross-sectioned. The surface of each cross-sectioned couple was polished using a 1 μ m diamond paste as the final step to ensure an even surface for microstructural and compositional analysis.

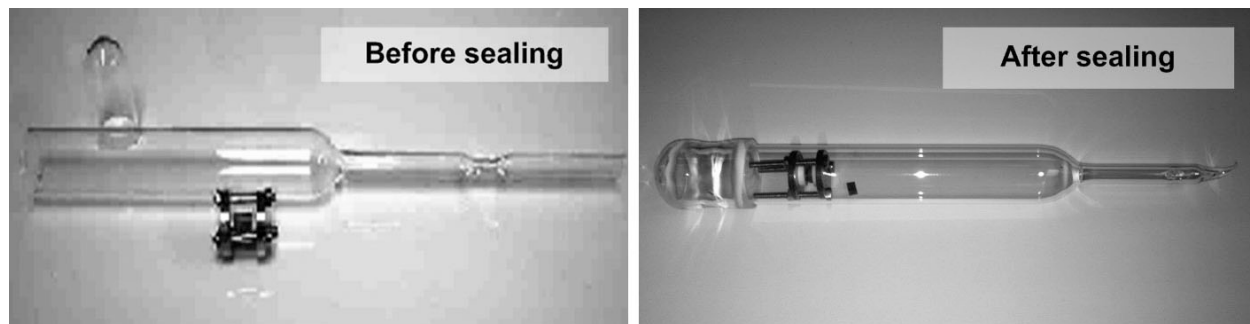
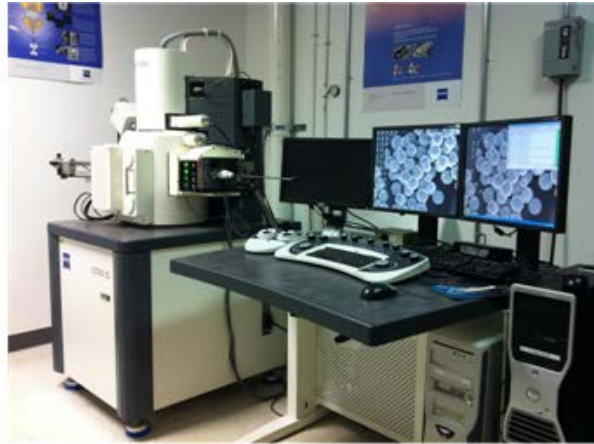


Figure 8. Quartz capsules for heat treatment of diffusion couples.

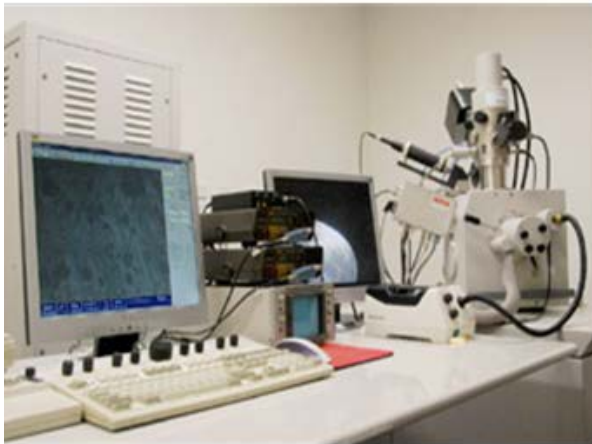
3.3 Characterization

For each diffusion couple, SEM (Zeiss ULTRA-55 FEG SEM) with an accelerating voltage of 20.0 kV was used to examine the quality of diffusion bonding and the thickness of the reaction layer. The BSE and SE micrographs were employed to observe metallurgical microstructures. The EDS was utilized for the semi-quantitative compositional analysis. A point-to-point counting measurement technique and ZAF correction were employed to determine compositional variation. TEM (FEI/Tecna™ F30) equipped with a HAADF detector (Fischione™) and XEDS was used to examine specified phases of the interdiffusion zone. Photographs of the SEM, FIB and TEM instruments are presented in Figure 9. Samples were prepared by FIB (FEI TEM200) as presented in Figure 10 for transmissions of electrons to be examined by TEM. SAED patterns were collected from selected regions of HAADF images and DF images to carry out crystallographic identification of intermetallic phases. In order to index the diffraction patterns, Digital Micrograph™, Microsoft Excel™, Microsoft Visual Studio™

and Photoshop™ were used.



(a)

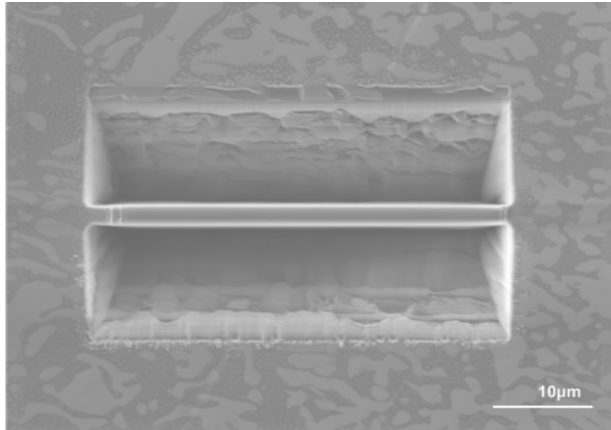


(b)

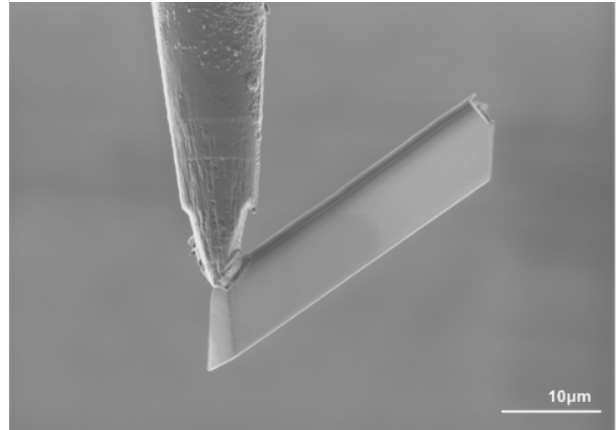


(c)

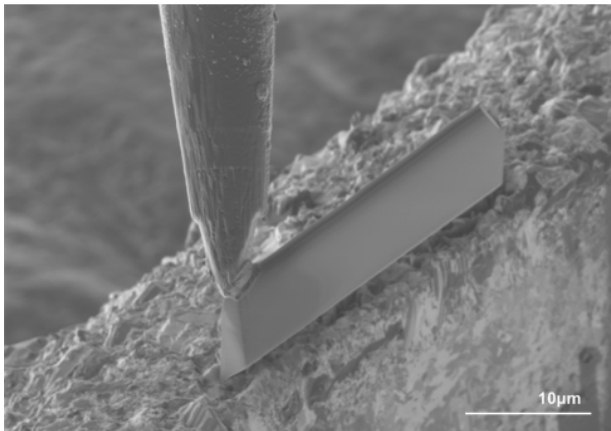
Figure 9. (a) Zeiss ULTRA-55 FEG SEM (b) FEI TEM200 FIB (c) FEI TECNAI F30 TEM.



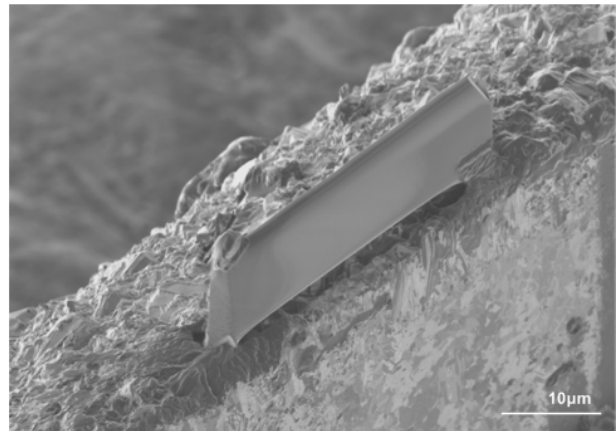
(a)



(b)



(c)



(d)

Figure 10. FIB sample preparation: (a) initial milling completion (b) in-situ lift-out (c) insertion of sample onto the pre-slotted Cu-grid (d) welding the sample on Cu-grid.

CHAPTER 4: RESULTS AND DISCUSSION

4.1. Microstructural and Compositional Development

The Interdiffusion microstructure development between diffusion couples U-Zr vs. Fe annealed at 630, 650 and 680°C for 96 hours is presented in Figure 11, Figure 12 and Figure 13, respectively. They all show a significant thickness with complex layered microstructural development.

Figure 11 presents the microstructure of the couple annealed at 630°C for 96 hours that contains the $ZrFe_2$, ϵ , and λ phases with highly DU-rich phase and U_6Fe phase as labeled. Although Nakamura reported the presence of χ phase below $895 \pm 10^\circ C$ [9], the couple annealed at 630°C had no χ phase. The total thickness of the reaction zone is around 53 μm .

The couples annealed at 650°C for 96 hours presented a larger interdiffusion reaction zone up to 94 μm . The $ZrFe_2$, χ , ϵ , and λ phases on the highly DU-rich and U_6Fe matrixes existed in the interdiffusion layers as presented in Figure 12. The χ phase, absent in the 630°C couple, was observed.

The couple annealed at 680°C for 96 hours had the largest interdiffusion reaction zone of 152 μm . The multi-phase layers, consisting of $ZrFe_2$, χ , ϵ , and λ phases with the highly DU-rich and U_6Fe matrixes, were observed in the interdiffusion layers as presented in Figure 13. The allotropic transformation of U between α -U(Orthorhombic) and β -U(Tetragonal) is predicted based on the U-Zr binary phase diagram.

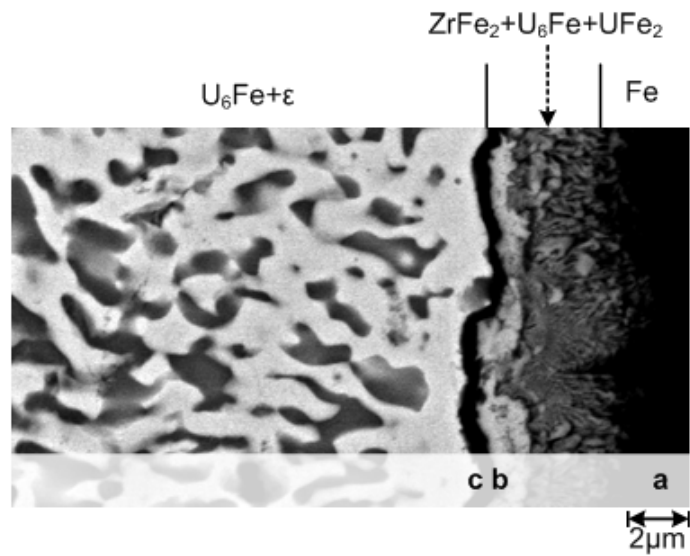
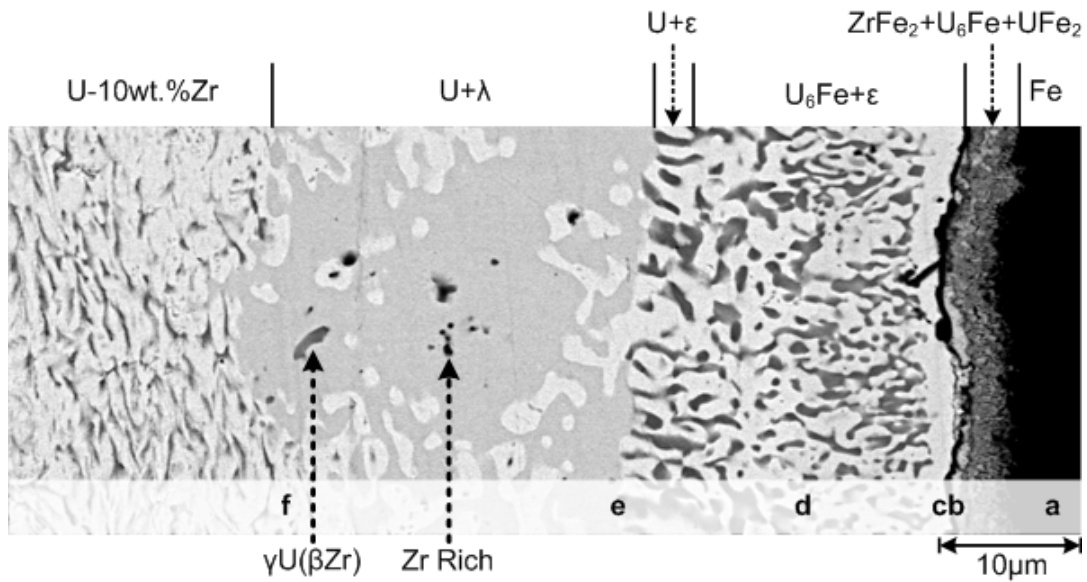


Figure 11. BSE micrographs of U-10 wt.% Zr vs. Fe diffusion couple annealed at 630°C for 96 hours.

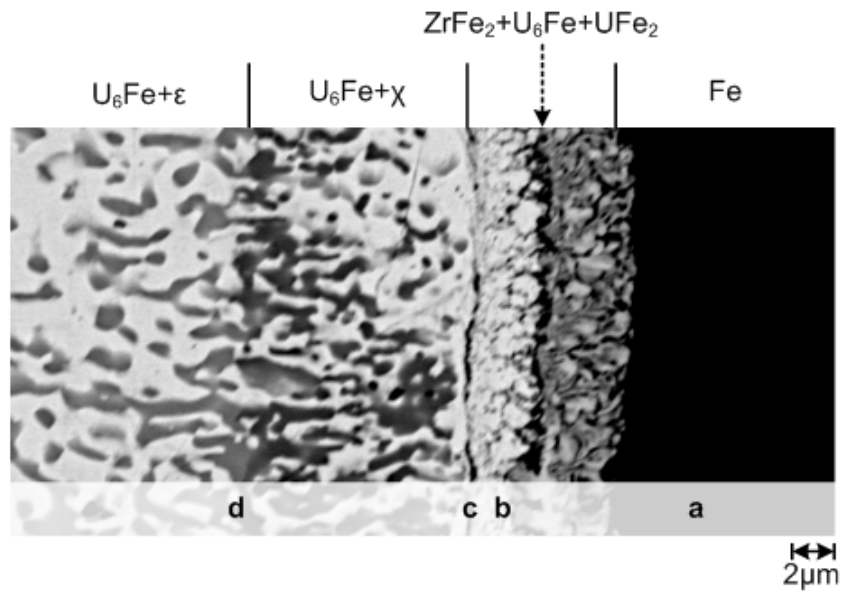
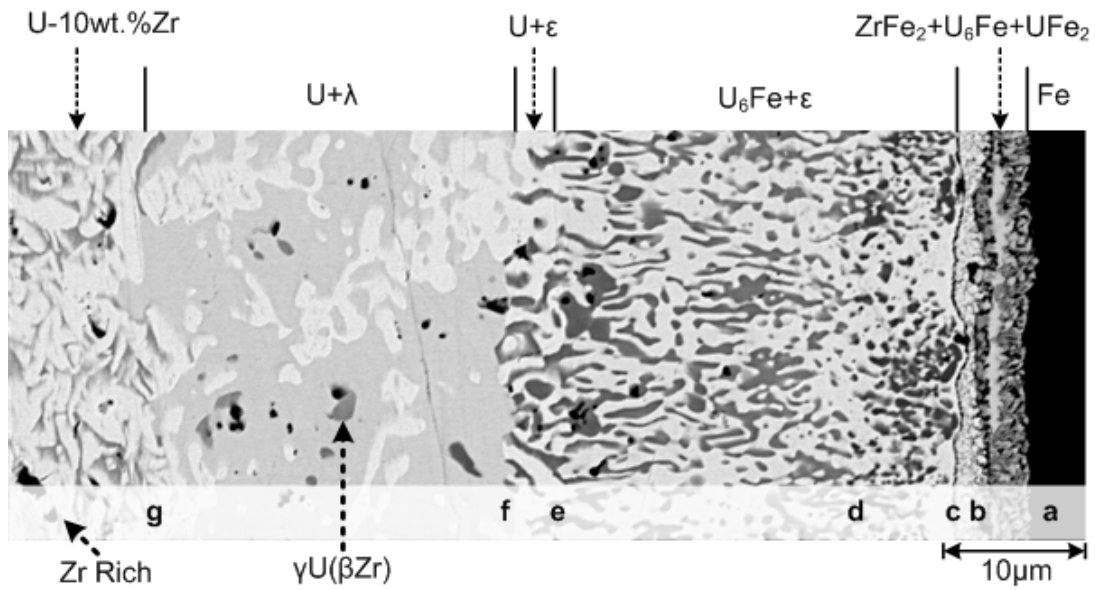


Figure 12. BSE micrographs of U-10 wt.% Zr vs. Fe diffusion couple annealed at 650°C for 96 hours.

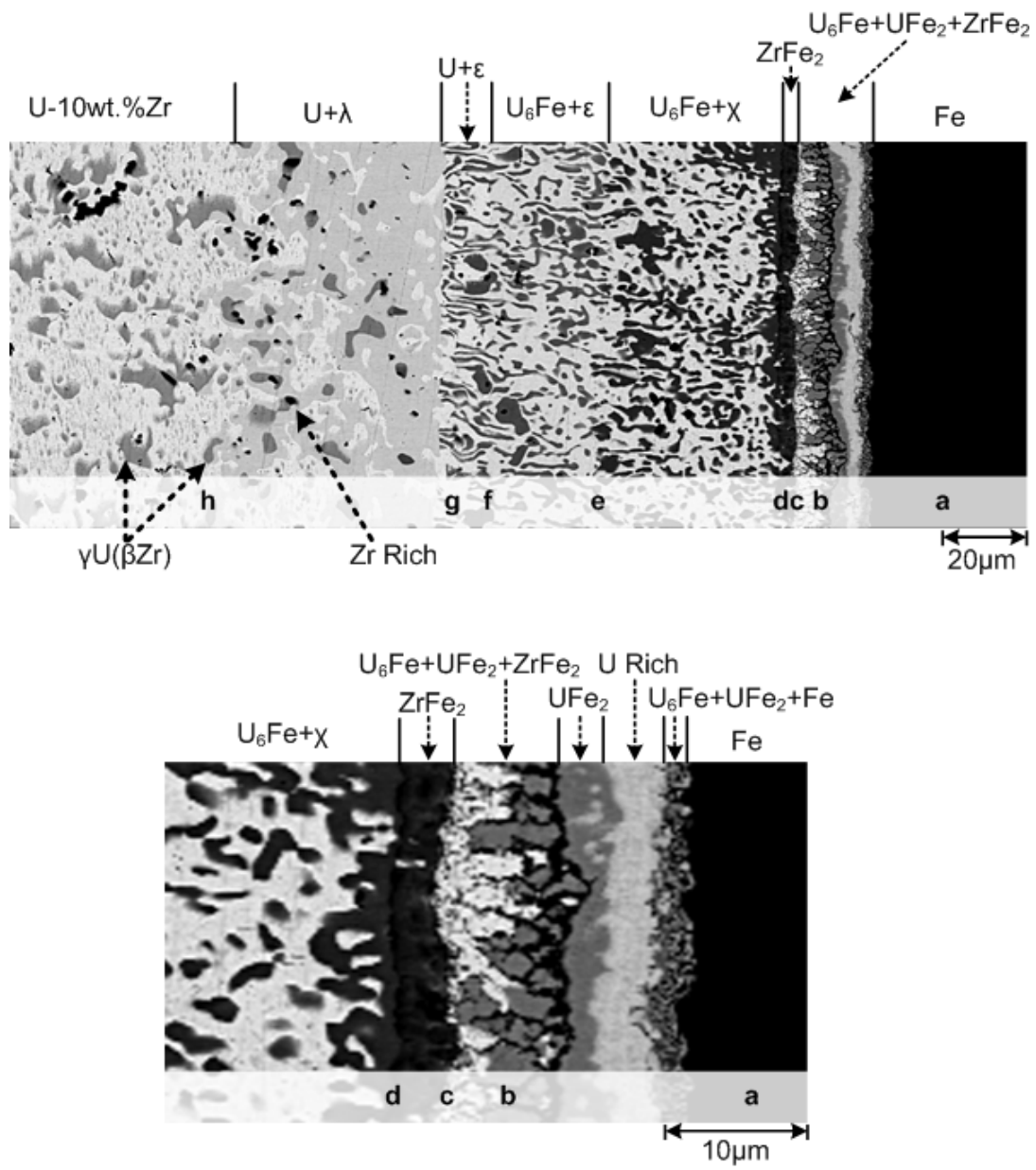


Figure 13. BSE micrographs of U-10 wt.% Zr vs. Fe diffusion couple annealed at 680°C for 96 hours.

Table 2 presents average composition of each phase observed in diffusion couple annealed at 680°C in this study. The couple annealed at 680°C is chosen for SEM-XEDS analysis since this couple at highest temperature produced the largest thickness and features for due consideration of SEM-XEDS resolution.

Table 2. Average composition of each phase observed in diffusion couple annealed at 680°C in this study (Unit: at.%).

Phase	Fe	Zr	U
UFe ₂	65.51	0	34.49
UFe ₆	14.94	1.38	83.67
ε	32.95	44.07	22.98
χ	50.07	32.71	17.23
λ	6.42	22.10	71.48
γ-U+βZr	0	64.40 ~57.04	42.96 ~ 35.61
Rich U	0.17	2.37	97.46
Rich Zr	0	95.65	4.35

Figure 14 presents isothermal ternary phase diagram of U-Zr-Fe system at 700°C with relevant phases of this diffusion study including intermetallic compounds such as U₆Fe, UFe₂, ZrFe₂, χ, ε and λ phases. Some of the layers adjacent to Fe were too thin for an accurate quantitative analysis due to the limits of XEDS resolution. Therefore, the compositions have

been estimated from correlating the BSE contrast and XEDS mapping shown in Figure 15. Particularly near the pure Fe, there are localized regions of Fe-depletion between the discontinuous ZrFe_2 phases, through which U appeared to have diffused preferentially to form U_6Fe in the matrix of UFe_2 phase. Overall, Zr-enriched regions corresponded to U-depleted region.

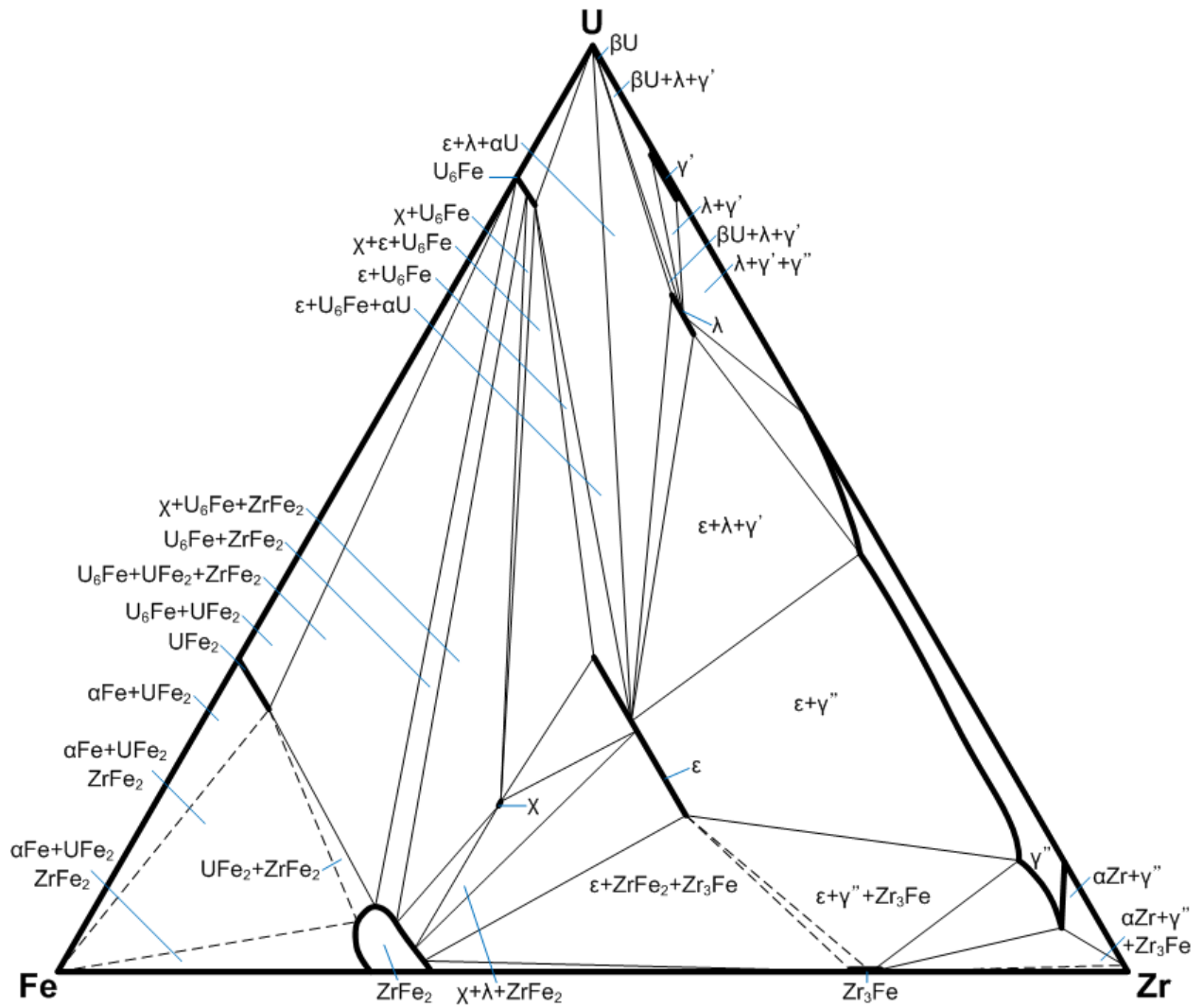


Figure 14. The isothermal ternary phase diagram of U-Zr-Fe system at 700°C [14].

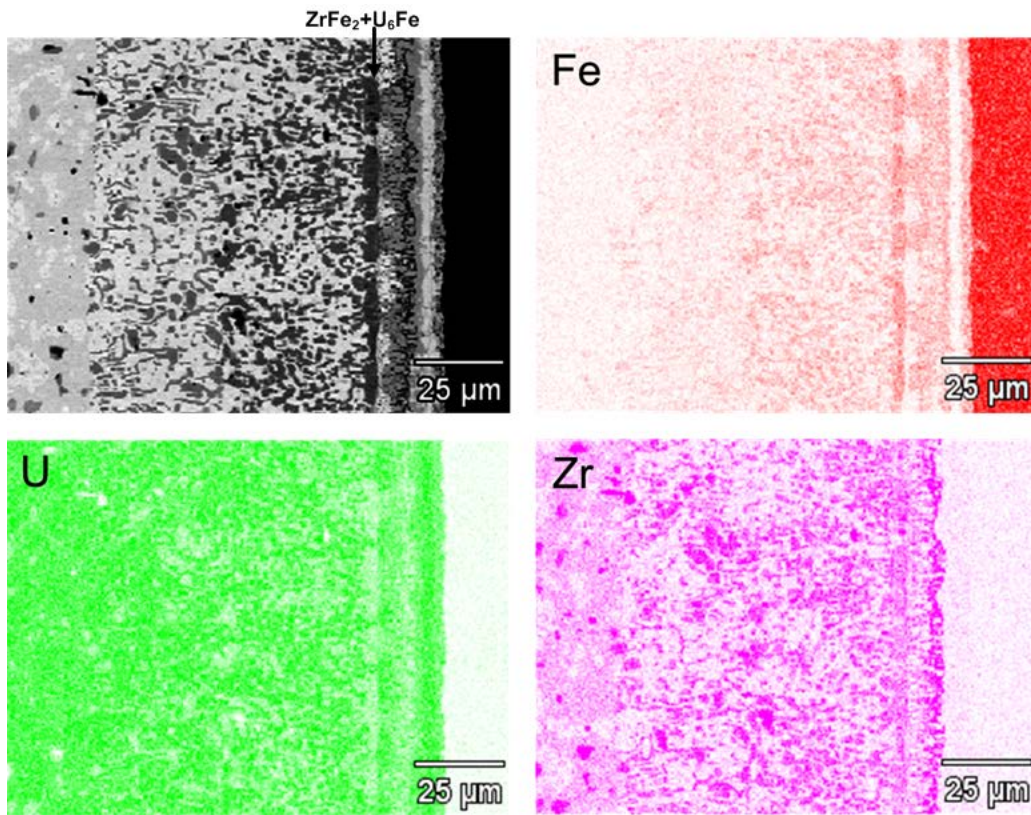


Figure 15. XEDS mapping for U, Zr and Fe in the U-10 wt.% Zr vs. Fe diffusion couple annealed at 680°C for 96 hours.

4.2. Diffusion Path of U-Zr vs. Fe System

The microstructural development of the reaction zone can be explained by the semi-quantitative diffusion path drawn on the isothermal phase diagram as shown in Figure 16, Figure 17, and Figure 18. In order to construct the diffusion path, the average compositions of the layers were estimated from the area fractions of each phase having approximate composition estimated

by SEM-XEDS. Overall, the estimated diffusion paths were similar for the temperature range investigated in this study. The layers of the microstructure labeled “a” through “f” in Figure 11, “a” through “g” in Figure 12, and “a” through “h” in Figure 13 correspond to the labeling “a” through “f” in Figure 16, “a” through “g” in Figure 17 and “a” through “h” in Figure 18, respectively. Details of phases present in each section of the diffusion path, corresponding to the microstructure, are reported in Table 3, Table 4 and Table 5. The estimated diffusion paths on the isothermal ternary phase diagram of U-Zr-Fe system demonstrated that Zr is a slower moving component because a significant interdiffusion occurs for U and Fe along the U-Fe binary side of the ternary triangle, before any diffusion of Zr is observed.

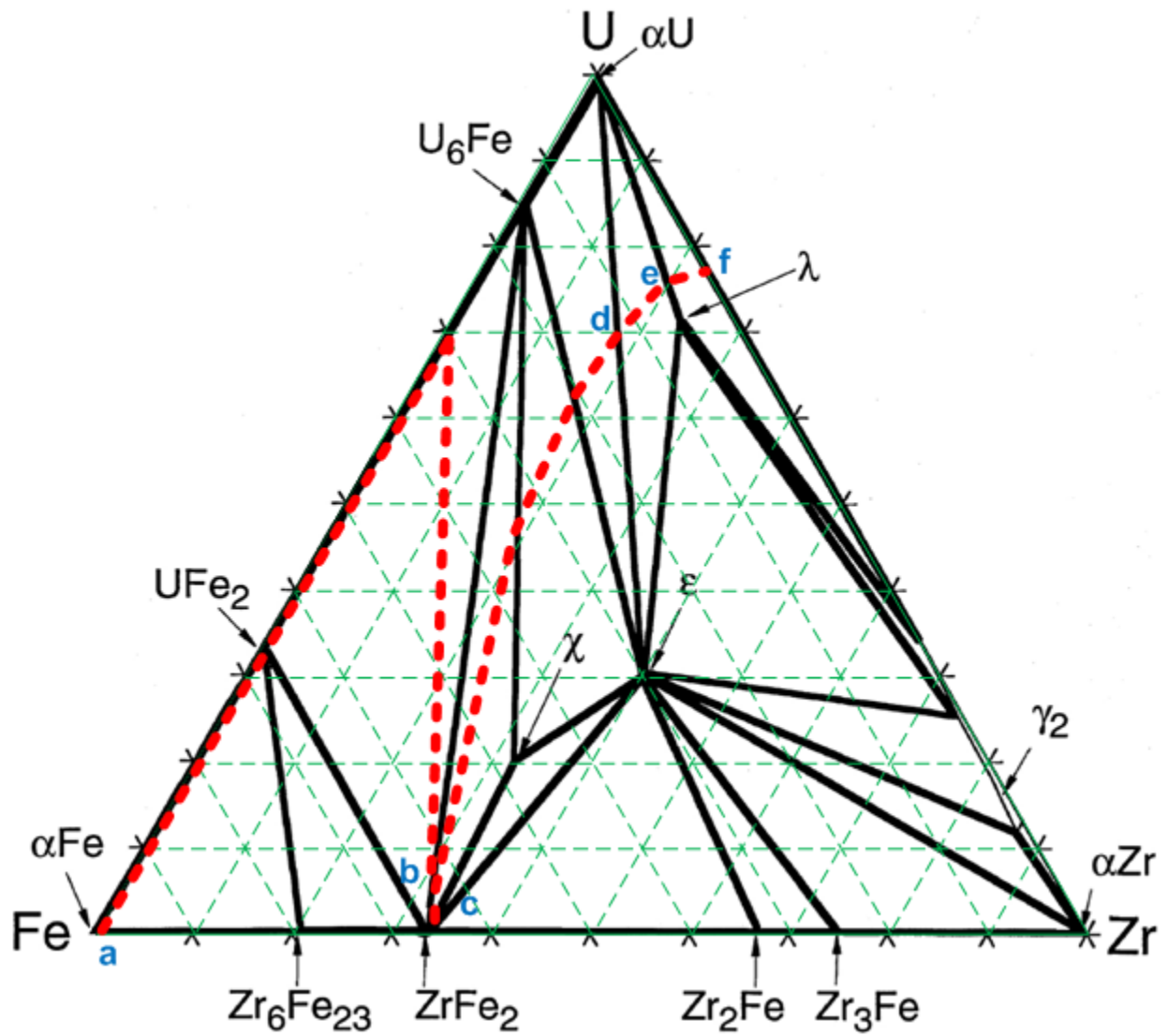


Figure 16. Estimated diffusion path of U-Zr vs. Fe diffusion couple annealed at 630°C for 96 hours plotted on the isothermal ternary phase diagram of the U-Zr-Fe system.

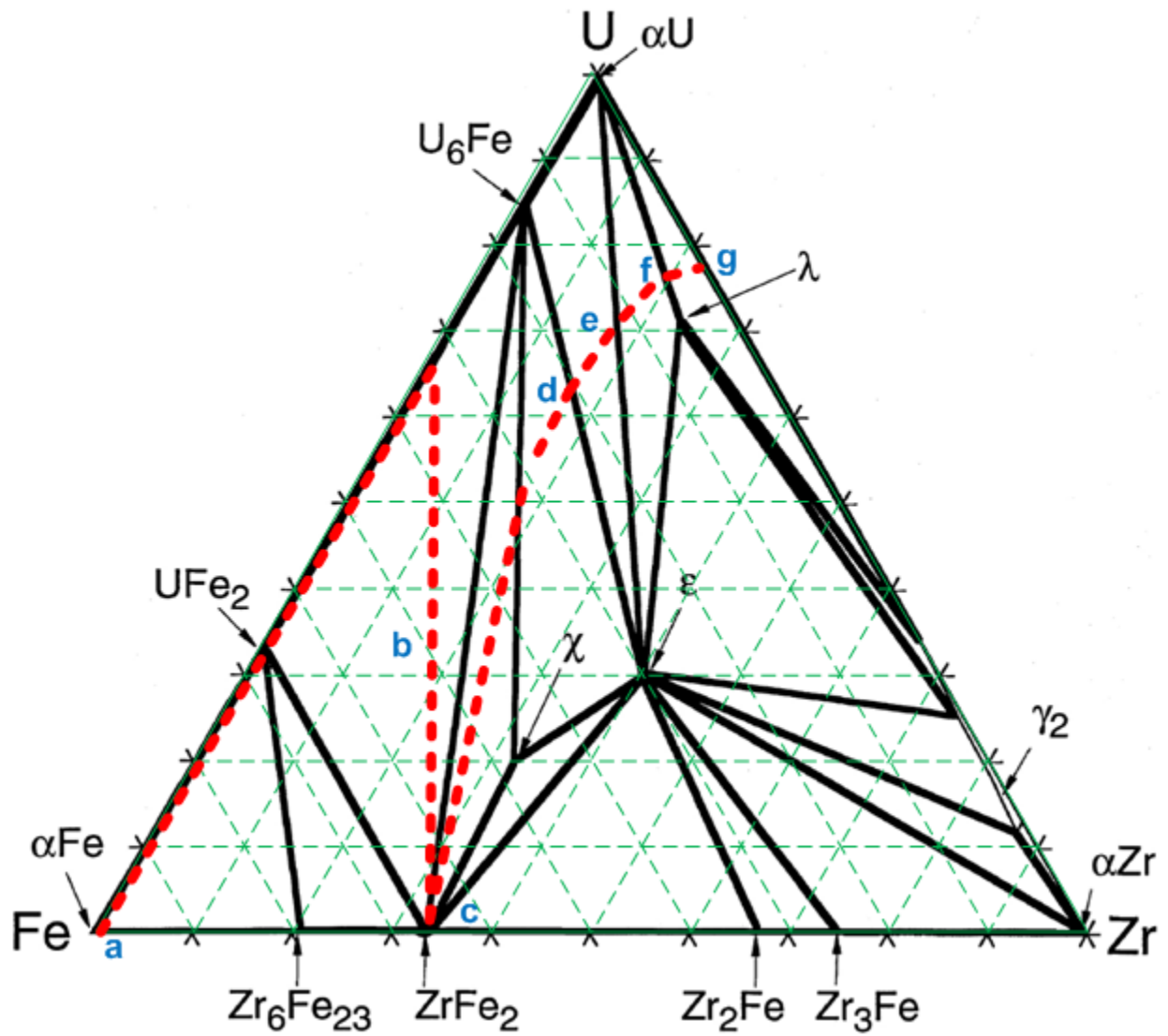


Figure 17. Estimated diffusion path of U-Zr vs. Fe diffusion couple annealed at 650°C for 96 hours plotted on the isothermal ternary phase diagram of the U-Zr-Fe system.

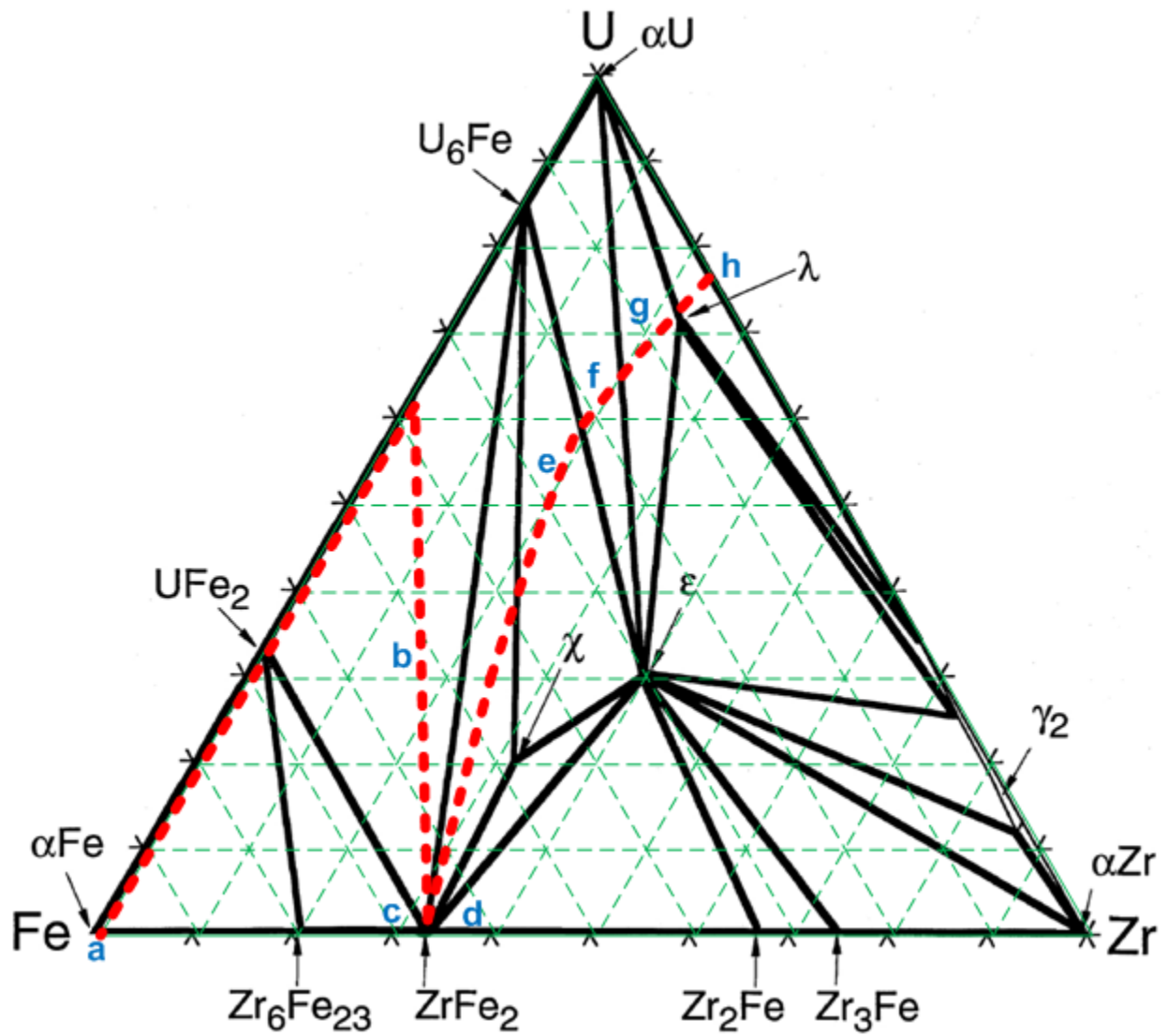


Figure 18. Estimated diffusion path of U-Zr vs. Fe diffusion couple annealed at 680°C for 96 hours plotted on the isothermal ternary phase diagram of the U-Zr-Fe system.

Table 3. Phases and phase number for each section of the diffusion path corresponding to the microstructure annealed at 630°C for 96 hours.

Section	Number of phases	Phases
a – b	4	Fe, Fe + UFe ₂ + U ₆ Fe + ZrFe ₂
b – c	1	ZrFe ₂
c – d	2	U ₆ Fe + ε
d – e	2	U-rich phase + ε
e – f	2	U-rich phase + λ

Table 4. Phases and phase number for each section of the diffusion path corresponding to the microstructure annealed at 650°C for 96 hours.

Section	Number of phases	Phases
a – b	4	Fe, Fe + UFe ₂ + U ₆ Fe + ZrFe ₂
b – c	3	UFe ₂ + U ₆ Fe + ZrFe ₂
c – d	3	ZrFe ₂ + U ₆ Fe + χ
d – e	2	U ₆ Fe + ε
e – f	2	U-rich phase + ε
f – g	2	U-rich phase + λ

Table 5. Phases and phase number for each section of the diffusion path corresponding to the microstructure annealed at 680°C for 96 hours.

Section	Number of phases	Phases
a – b	4	Fe, Fe + UFe ₂ + U ₆ Fe + ZrFe ₂
b – c	3	UFe ₂ + U ₆ Fe + ZrFe ₂
c – d	3	ZrFe ₂
d– e	2	U ₆ Fe + χ
e– f	2	U ₆ Fe + ε
f– g	2	U-rich phase + ε
g– h	2	U-rich phase + λ

4.3. Growth of Interdiffusion Microstructure in U-10 wt.% Zr vs. Fe Diffusion Couples

The interdiffusion zone was distinguished into three layers, A, B and C, to calculate the growth constants and activation energies. Layer A includes the several thin reaction layers adjacent to Fe. Layer B includes the χ and ε phases in the matrix of U₆Fe and U solid solution. Layer C includes the λ phase in the matrix of U solid solution. The identified phases in each layer are summarized in Table 6 and Figure 19. It should be note that at 680°C, U solid solution should exist as β -U (tP30) as indicated in Table 6.

Table 6. Phases in reaction layers distinguished for determination of growth constants.

Layer	630°C	650°C	680°C
Fe	α -Fe	α -Fe	α -Fe
Layer A	$U_6Fe + UFe_2 + ZrFe_2$	$U_6Fe + UFe_2 + ZrFe_2$	$U_6Fe + UFe_2 + ZrFe_2$
Layer B	$\alpha-U + U_6Fe + \varepsilon$	$\alpha-U + U_6Fe + \chi + \varepsilon$	$\beta-U + U_6Fe + \chi + \varepsilon$
Layer C	$\alpha-U + \lambda$	$\alpha-U + \lambda$	$\beta-U + \lambda$
U-10 wt.% Zr	$\alpha-U + \gamma_2$	$\alpha-U + \gamma_2$	$\beta-U + \gamma_2$

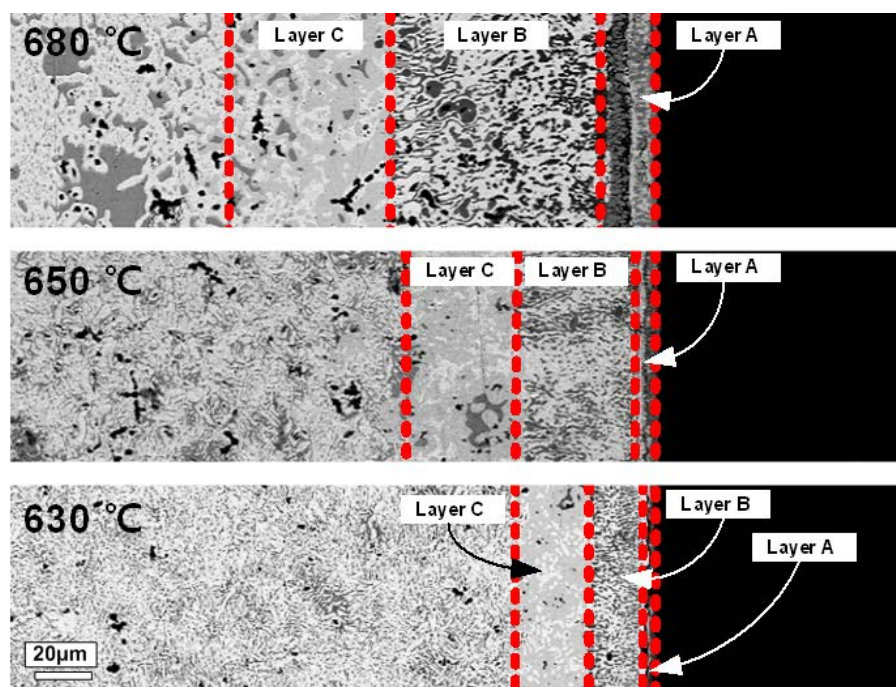


Figure 19. Thicknesses of each distinguished layer developed in diffusion couples, U-10 wt.% Zr vs. Fe diffusion couples annealed at 630, 650 and 680°C for 96 hours.

Table 7 reports the thickness for each layer as a function of temperature. These thicknesses were averaged from at least 12 random location measurements for each layer. The growth constant was calculated by assuming diffusion controlled parabolic growth using the relation:

$$x = \sqrt{2 \cdot t \cdot k_p} \quad (1)$$

where x (m) is the thickness of the layer, t (s) is the annealed time and $k_p(\text{m}^2\text{s}^{-1})$ is the growth constant. The parabolic growth constants obey the Arrhenius relationship. Therefore, the activation energy for each layer was calculated using the relation:

$$k_p = k_0 e^{\left(\frac{-Q}{RT}\right)} \quad (2)$$

where k_0 is a constant, Q ($\text{kJ}\cdot\text{mol}^{-1}$) is the activation energy, R ($\text{J}\cdot\text{mol}^{-1}\cdot\text{K}^{-1}$) is the ideal gas constant and T (K) is the anneal temperature. Table 8 shows the growth constants and the activation energy for each layer. Layer A has the highest activation energy and Layer C has the lowest activation energy.

Table 7. Thicknesses of each interdiffusion layer measured from diffusion couples, U-10 wt.% Zr vs. Fe diffusion couples annealed at 630, 650 and 680°C for 96 hours.

T(°C)	Anneal time (hours)	Layer A (μm)	Layer B (μm)	Layer C (μm)	Total (μm)
630	96	3.81	23.50	27.40	52.95
650	96	8.34	47.69	38.54	94.17
680	96	17.22	79.39	56.36	151.68

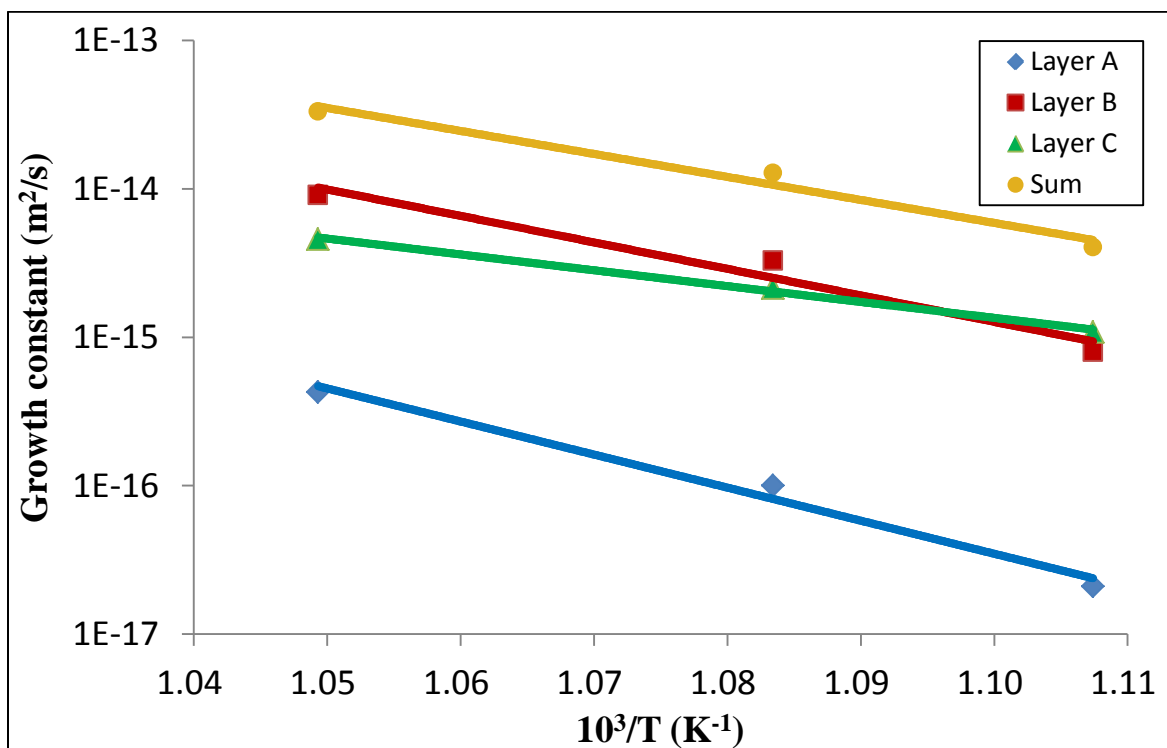


Figure 20. Arrhenius plot of parabolic growth constant for each interdiffusion layer from diffusion couples, U-10 wt.% Zr vs. Fe diffusion couples annealed at 630, 650 and 680°C for 96 hours.

Table 8. The growth constants and activation energies of each interdiffusion layer from diffusion couples, U-10 wt.% Zr vs. Fe diffusion couples annealed at 630, 650 and 680°C for 96 hours.

Layer		630°C	650°C	680°C
Layer A	k (m ² /s)	2.1×10^{-17}	8.0×10^{-16}	1.1×10^{-15}
	Q (kJ/mol)	431.7		
Layer B	k (m ² /s)	1.0×10^{-16}	3.3×10^{-15}	2.2×10^{-15}
	Q (kJ/mol)	348.4		
Layer C	k (m ² /s)	4.3×10^{-16}	9.1×10^{-15}	4.6×10^{-15}
	Q (kJ/mol)	205.8		
Total	k (m ² /s)	4.1×10^{-15}	1.3×10^{-14}	3.3×10^{-14}
	Q (kJ/mol)	301.2		

4.4. Crystallographic Analysis of Ternary Intermetallic Phases

Although the χ , ε and λ phases in the interdiffusion microstructure have been reported by several investigators, their crystal structures and potential stoichiometry have not been reported. Based on BSE of diffusion couple annealed at 680°C shown in Figure 21(a), FIB-INLO was carried out on several samples as shown in Figure 21(b ~ d) that contained one or two phases of the ternary intermetallic χ , ε and λ phases.

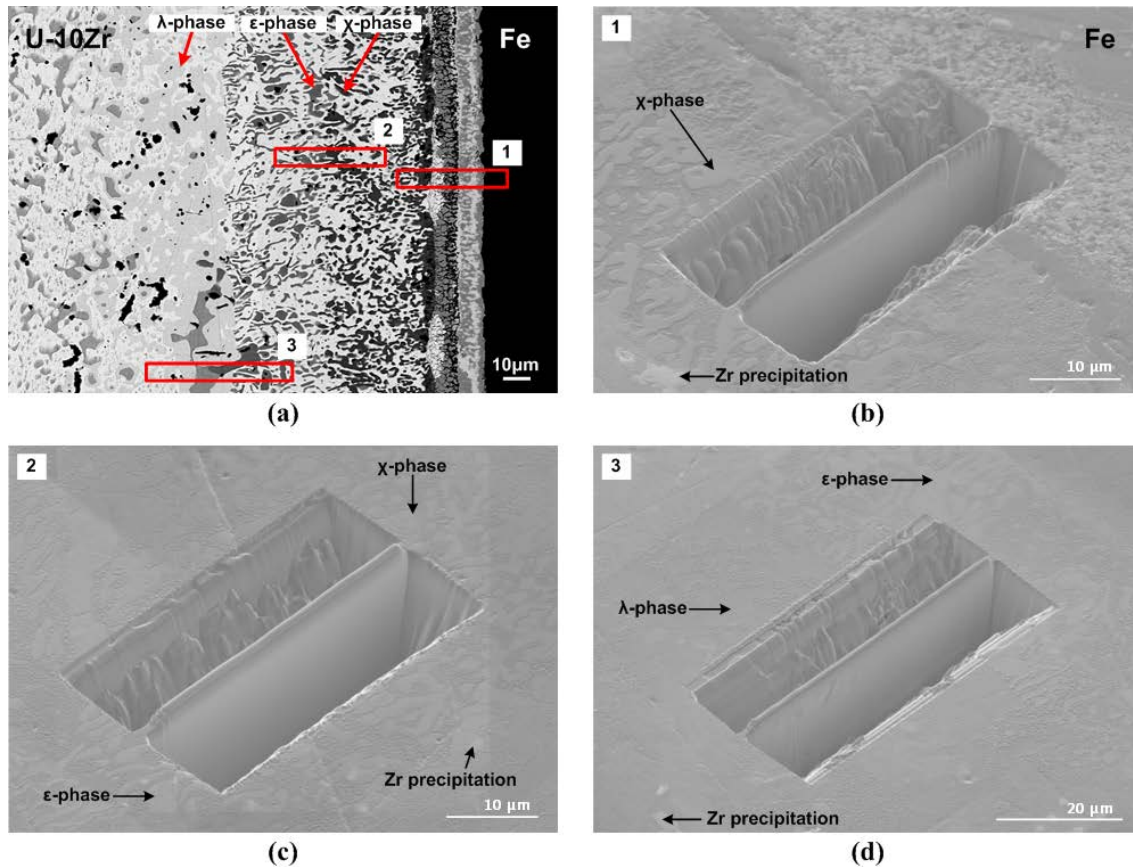
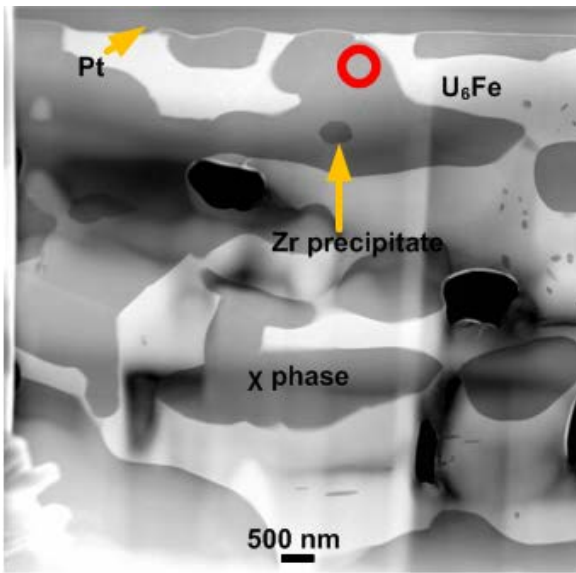


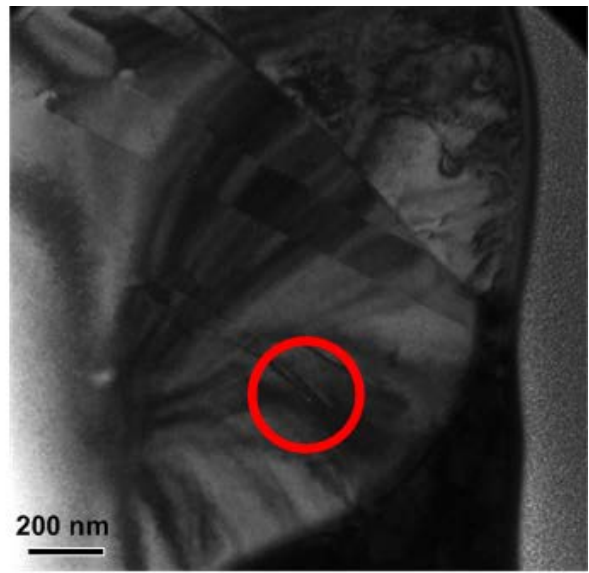
Figure 21. U-Zr vs. Fe diffusion couples annealed at 680°C for 96 hours: (a) typical BSE micrograph and FIB preparations for TEM studies (b) for χ phase and several layers near Fe side, (c) for χ and ϵ phase, and (d) ϵ and λ phase.

The HAADF STEM, DF and SAED from the χ , ϵ and λ phases are presented in Figure 22, Figure 23 and Figure 24 respectively. Each HAADF STEM micrograph in Figure 22(a), Figure 23(a) and Figure 24(a) was specifically prepared by FIB-INLO to contain one or two phases of the three intermetallics. The red circles in HAADF STEM and DF of Figure 22(a and b), Figure 23(a and b) and Figure 24(a and b) indicate the positions at which the electron

diffraction pattern presented in Figure 22(c and d), Figure 23(c and d) and Figure 24(c and d) were collected using multiple zone-axes. Based on the electron diffraction patterns, the three phases were identified as orthorhombic χ , tetragonal ε and tetragonal λ as listed in Table 9. The crystal structure and the lattice parameters of χ , ε and λ phases were analogous to FeZr, FeZr₂ and U₃Si phases, respectively. Composition of each phase was also measured by TEM-XEDS with better resolution as reported in Table 10. Therefore, the chemical formulae were estimated as extended solid solution of binary intermetallics, namely Fe(Zr,U), Fe(Zr,U)₂ and U₃(Zr,Fe), for the χ , ε and λ phases, respectively.



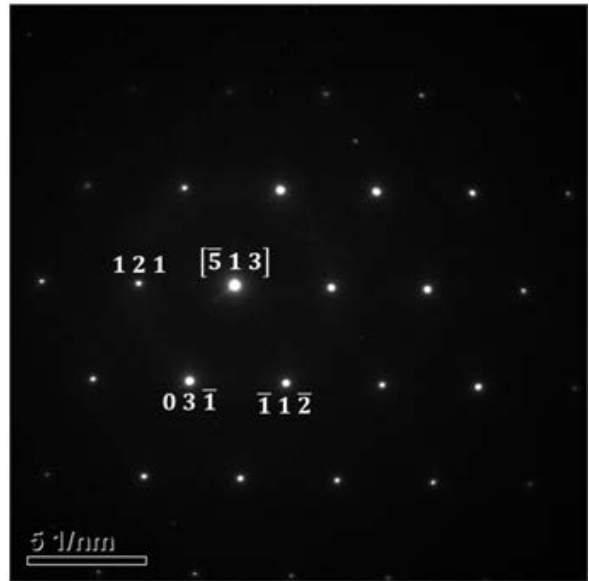
(a)



(b)

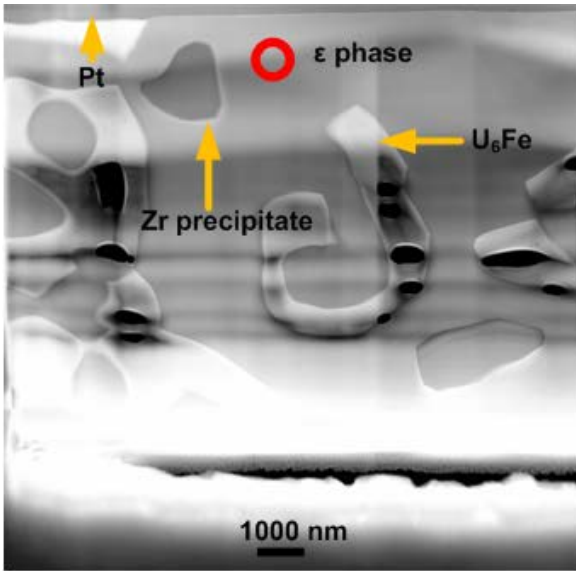


(c)

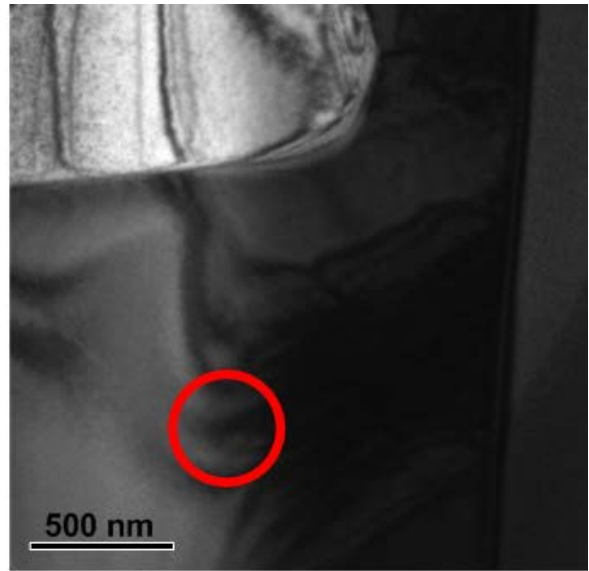


(d)

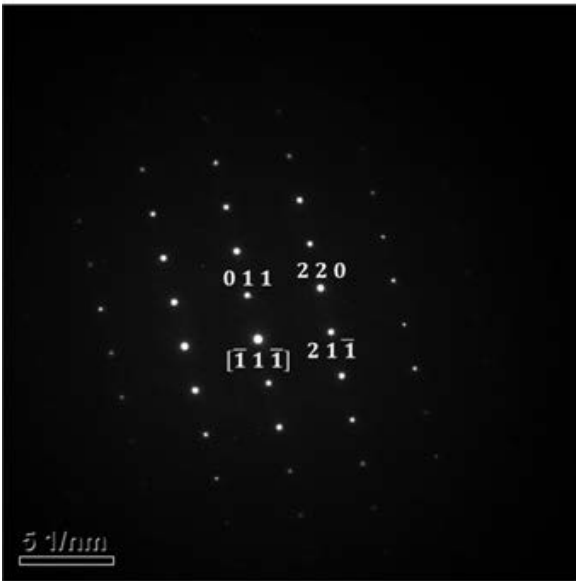
Figure 22. The χ phase developed in the U-Zr vs. Fe diffusion couple annealed at 680°C: (a) HAADF STEM micrograph, (b) DF micrograph, and (c) SAED along the $[1\ 1\ \bar{1}]$, and (d) $[\bar{5}\ 1\ 3]$ beam directions.



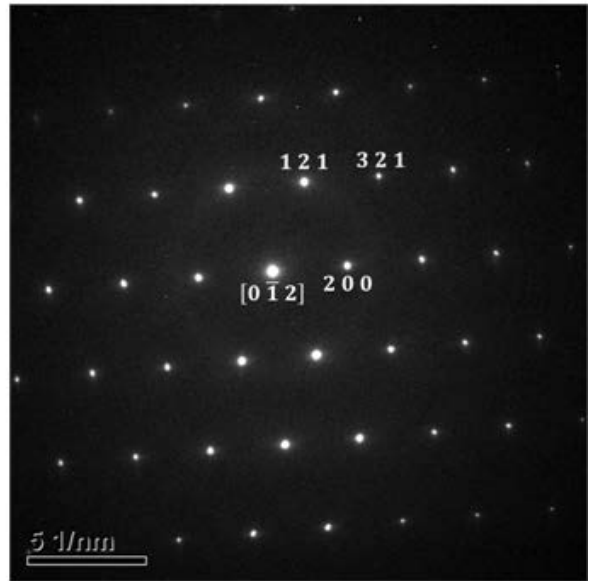
(a)



(b)

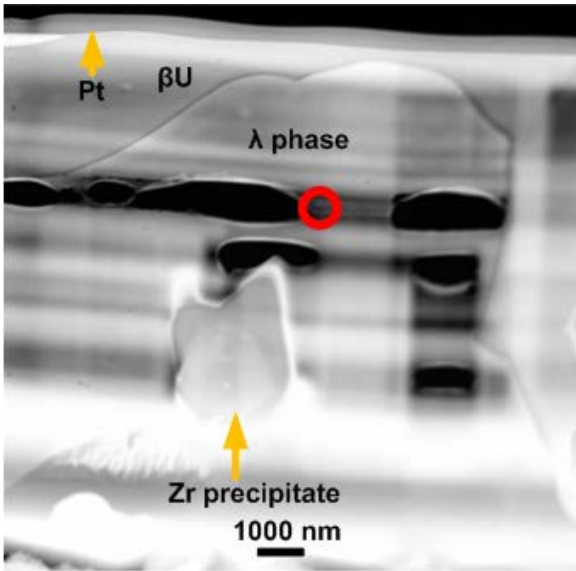


(c)

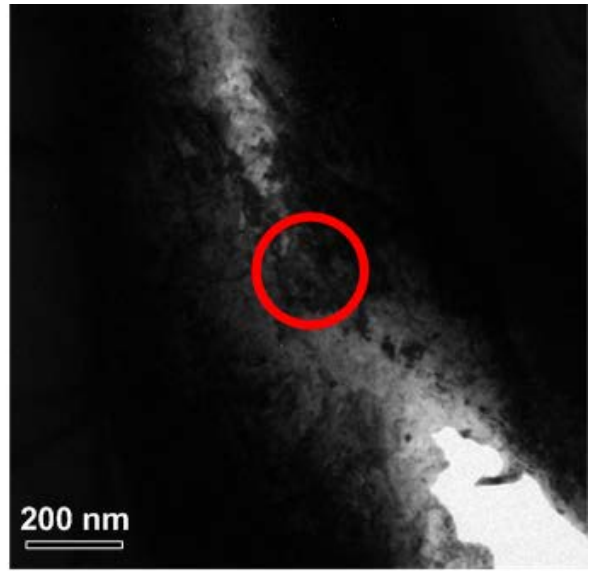


(d)

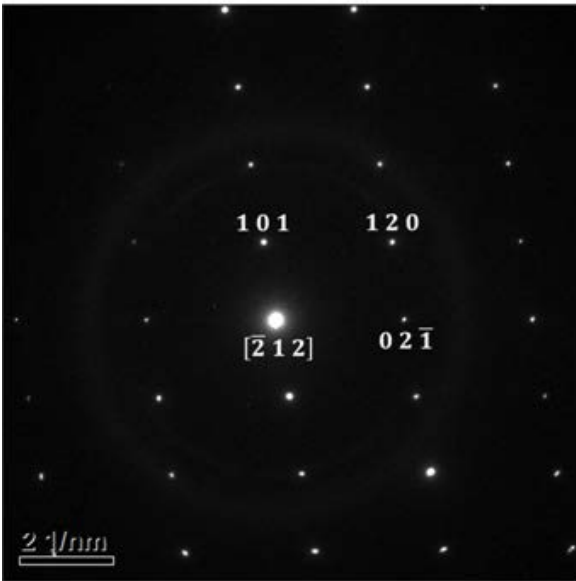
Figure 23. The ϵ phase developed in the U-Zr vs. Fe diffusion couple annealed at 680°C: (a) HAADF STEM micrograph, (b) DF micrograph, and (c) SAED along the $[\bar{1} 1 \bar{1}]$ and (d) $[0 \bar{1} 2]$ beam directions.



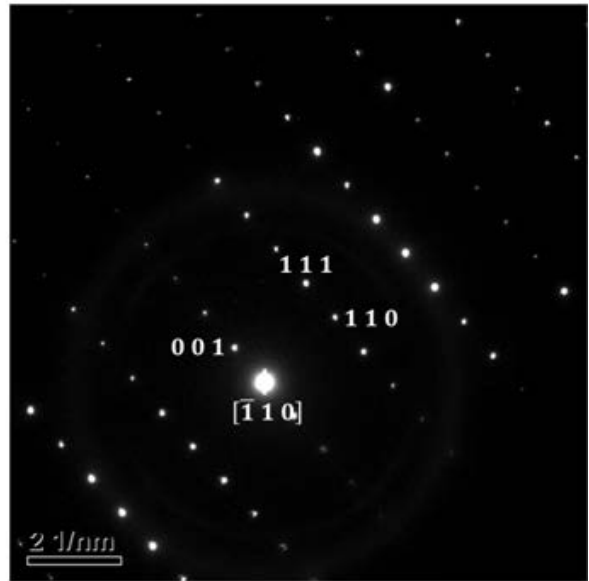
(a)



(b)



(c)



(d)

Figure 24. The λ phase developed in the U-Zr vs. Fe diffusion couple annealed at 680°C: (a) HAADF STEM micrograph, (b) DF micrograph, and (c) SAED along the $[\bar{2} 1 2]$ and (d) $[\bar{1} 1 0]$ beam directions.

Table 9. Crystallographic information of the χ , ε and λ phases.

χ	Pearson Symbol	oP8
	$a \times b \times c$ (Å)	$4.854 \times 7.062 \times 5.376$
	$\alpha \times \beta \times \gamma$ (°)	$90 \times 90 \times 90$
	Space group	Pnma (62)
	Chemical formula	Fe(Zr,U)
ε	Pearson Symbol	tI12
	$a \times b \times c$ (Å)	$6.385 \times 6.385 \times 5.596$
	$\alpha \times \beta \times \gamma$ (°)	$90 \times 90 \times 90$
	Space group	I4/mcm (140)
	Chemical formula	Fe(Zr,U) ₂
λ	Pearson Symbol	tI16
	$a \times b \times c$ (Å)	$7.264 \times 7.264 \times 10.537$
	$\alpha \times \beta \times \gamma$ (°)	$90 \times 90 \times 90$
	Space group	I4/mcm (140)
	Chemical formula	U ₃ (Zr,Fe)

Table 10. Chemical composition measured by SEM-XEDS and TEM-XEDS for the χ , ε and λ phases (unit: at.%).

	χ			ε			λ		
	U	Zr	Fe	U	Zr	Fe	U	Zr	Fe
TEM-XEDS	22	34	44	30	43	27	76	19	5
SEM-XEDS	17	33	50	23	44	33	72	22	6
Previous study[15]	18	32	50	17~34	33~50	33	69~73	21~25	6

CHAPTER 5: SUMMARY

Microstructures and phase constituents within the diffusional interaction layer of the diffusion couple, U-10 wt.% Zr vs. Fe, annealed at 630, 650, and 680°C, were examined by BSE and XEDS. In addition, the analyses of HAADF, DF and SAED via TEM were employed for the crystallographic determination of χ , ε and λ phases for the first time.

- The interdiffusion microstructure of U-10 wt.% Zr vs. Fe diffusion couples consisted of multiple layers containing several phases such as χ , ε , λ , ZrFe_2 , UFe_2 with U_6Fe and DU-rich matrixes.
- The average compositions through the interaction layer were systematically determined, and employed to construct a semi-quantitative diffusion path on isothermal U-Zr-Fe ternary phase diagrams. They showed qualitatively the diffusional behavior of elements. U was a faster moving component on the Fe side than Zr. Zr was the slow diffusion specie in the U-Zr vs. Fe diffusion couples.
- The reaction zone was distinguished into layer A ($\text{U}_6\text{Fe} + \text{UFe}_2 + \text{ZrFe}_2$), layer B (DU-rich + $\text{U}_6\text{Fe} + \chi + \varepsilon$) and layer C (DU-rich + λ). The thickness for each layer was measured at each temperature, and employed to calculate the parabolic growth constant. From the parabolic growth constants determined, the activation energy of growth for each layer was calculated using Arrhenius relationship as given below:
 - Layer A = 431.7 kJ/mol
 - Layer B = 348.4 kJ/mol

- Layer C = 205.8 kJ/mol.
- For the first time, the crystallographic identifications of orthorhombic- χ , tetragonal- ϵ and tetragonal- λ , were carried out from several electron diffraction patterns with multiple zone-axes. The exact crystal structure and composition of χ , ϵ and λ -phases were identified as oP8 Pnma(62) Fe(Zr,U), tI12 I4/mcm(140) Fe(Zr,U)₂, and tI16 I4/mcm(140) U₃(Zr,Fe), respectively.

**APPENDIX: MATHEMATICAL THEOREM FOR RECIPROCAL
LATTICE**

In order to complete the crystallographic identification for χ , ε and λ , the comparisons of theoretical results with experimental results were used in this research. The theoretical results were derived from calculating the spacing and angle of the reciprocal lattice. Otherwise, the experimental results were derived from measurement of the spacing and angle of the reciprocal lattice in the electron diffraction patterns. Figure 25 shows computational mechanism, which was used in this research for identification of these phases.

The original interplanar spacing (d_{hkl}) can be expressed by the reciprocal lattice vectors, \mathbf{a}^* , \mathbf{b}^* and \mathbf{c}^* :

$$d_{hkl} = \frac{1}{|\mathbf{h}\mathbf{a}^* + \mathbf{k}\mathbf{b}^* + \mathbf{l}\mathbf{c}^*|} \quad (\text{A.1})$$

$$\begin{aligned} & |\mathbf{h}\mathbf{a}^* + \mathbf{k}\mathbf{b}^* + \mathbf{l}\mathbf{c}^*|^2 \\ &= (h^2\mathbf{a}^{*2} + k^2\mathbf{b}^{*2} + l^2\mathbf{c}^{*2} + 2klb^*c^*\cos\alpha^* + 2lhc^*a^*\cos\beta^* \\ &+ 2hka^*b^*\cos\gamma^*) \end{aligned} \quad (\text{A.2})$$

The original interplanar angle is:

$$\begin{aligned} \cos \varphi = d_{hkl} d_{h'k'l'} [hh' a^{*2} + kk' b^{*2} + ll' c^{*2} + (kl' + lk') b^* c^* \cos \alpha^* \\ + (hl' + lh') a^* c^* \cos \beta^* + (hk' + kh') a^* b^* \cos \gamma^*] \end{aligned} \quad (\text{A.3})$$

Orthorhombic:

Orthorhombic interplanar spacing square is derived from (A.1) and (A.2):

$$d_{hkl}^2 = \frac{1}{h^2 a^{*2} + k^2 b^{*2} + l^2 c^{*2}} \quad (\text{A.4})$$

Orthorhombic interplanar angle is derived from (A.3):

$$\cos \varphi = d_{hkl} d_{h'k'l'} [hh' a^{*2} + kk' b^{*2} + ll' c^{*2}] \quad (\text{A.5})$$

where:

$$\alpha^* = \beta^* = \gamma^* = 90^\circ$$

$$a^* = \frac{1}{a}, \quad b^* = \frac{1}{b}, \quad c^* = \frac{1}{c}$$

Tetragonal:

Tetragonal interplanar spacing square is derived from (A.1) and (A.2):

$$d_{hkl}^2 = \frac{1}{(h^2 + k^2) a^{*2} + l^2 c^{*2}} \quad (\text{A.6})$$

Tetragonal interplanar angle is derived from (A3):

$$\cos \varphi = d_{hkl} d_{h'k'l'} [(hh' + kk') b^{*2} + ll' c^{*2}] \quad (\text{A.7})$$

where:

$$\alpha^* = \beta^* = \gamma^* = 90^\circ$$

$$a^* = b^*$$

$$a^* = \frac{1}{a}, \quad c^* = \frac{1}{c}$$

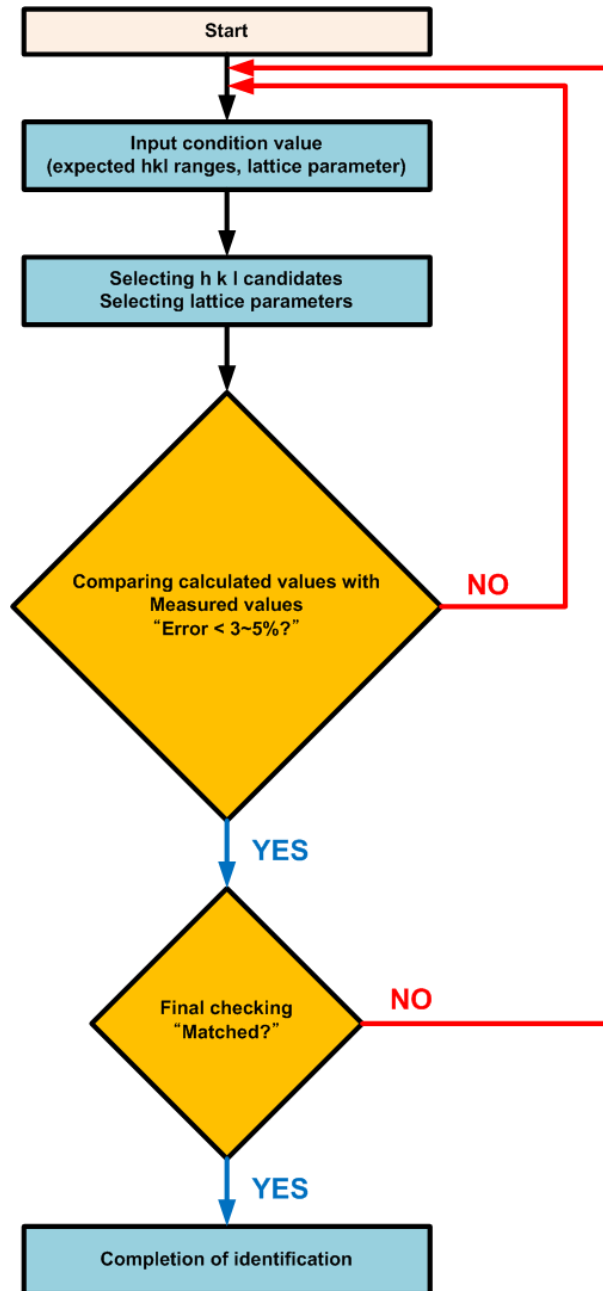


Figure 25. The procedure C++ coding for the identification of crystal structure and indexing

REFERENCE

- [1] S. US Department of Energy & Office of Nuclear Energy, and Technology, (2006).
- [2] Idaho National Laboratory, 1 (2007).
- [3] U.D.o.E.O.o.N. Energy, 1 (2007).
- [4] G.L. Hofman, L.C. Walters, T.H. Bauer, Progress in Nuclear Energy, 31 (1997) 83-110.
- [5] Y.S. Kim, S.L. Hayes, G.L. Hofman, A.M. Yacout, Journal of Nuclear Materials, 359 (2006) 17-28.
- [6] A.I. Leipunskii, O.D. Kazachkovskii, I.I. Afrikantov, M.S. Pinkhasik, N.V. Krasnoyarov, M.S. Poido, At Energy, 17 (1964) 1090-1093.
- [7] S.F. Mughabghab, IAEA, (2003) 32.
- [8] K. Huang, Y. Park, A. Ewh, B.H. Sencer, J.R. Kennedy, K.R. Coffey, Y.H. Sohn, Journal of Nuclear materials, 424 (2012) 82-88.
- [9] K. Nakamura, T. Ogata, M. Kurata, A. Itoh, M. Akabori, Journal of Nuclear materials, 275 (1999) 246-254.
- [10] T. Ogata, M. Kurata, K. Nakamura, A. Itoh, M. Akabori, Journal of Nuclear materials, 250 (1997) 171-175.
- [11] D.D. Keiser Jr, M.A. Dayananda, Journal of Nuclear materials, 200 (1993) 229-243.
- [12] D.D.a.D.M.A. Keiser Jr, Metallurgical and Materials Transactions A, 25A (1994).
- [13] K. Nakamura, M. Kurata, T. Ogata, A. Itoh, M. Akabori, Journal of Nuclear materials, 275 (1999) 151-157.
- [14] O. Fabrichnaya, Non-Ferrous Metal System, 11C4 (2007).

[15] H. Okamoto, *Journal of Phase Equilibria and Diffusion*, 28 (2007) 499-500.